

**Ultrafast dynamics of carriers, coherent acoustic phonons and strain pulses
in BiSbTe_{1.5}Se_{1.5} topological insulator thin films**

Anupama Chauhan,¹ Sidhanta Sahu,¹ Poulami Ghosh,¹ Dheerendra Singh,¹ Sambhu G
Nath,¹ Anjan Kumar N M,¹ P.K. Panigrahi,^{1,2} Chiranjib Mitra,¹ and N. Kamaraju*

¹*Department of Physical Sciences, Indian Institute of Science Education and Research Kolkata,
Mohanpur, 741246, West Bengal, India.*

²*Centre for Quantum Science and Technology,
Siksha 'O' Anusandhan university, Bhubaneswar, 751030, Odisha, India.*

(Dated: March 4, 2025)

Abstract

We investigate the ultrafast carrier, coherent acoustic phonons (CAPs), and acoustic strain pulse dynamics in topological insulator $\text{BiSbTe}_{1.5}\text{Se}_{1.5}$ (BSTS) thin films of varying thickness using degenerate pump-probe reflection spectroscopy. Here, Sapphire has been chosen as the main substrate due to its maximum acoustic reflectivity at the BSTS-sapphire interface compared to BSTS-GaAs, BSTS-Si, and BSTS-MgO interfaces. For the films with thickness more than twice the penetration depth, the transient reflectivity data predominantly exhibits travelling acoustic strain pulses (TASP) on the top of single-exponential electronic decay (~ 2 ps). In contrast, films with thickness less than penetration depth are dominated by CAPs and a bi-exponential electronic background with decay constants $\tau_1 \sim 2$ ps and $\tau_2 \sim 260\text{-}380$ ps. The observed TASP dynamics are well-described by a theoretical acoustic strain model. Further, to elucidate the underlying physical mechanisms governing the behaviour of photo-excited carriers, CAPs, and strain pulses, we performed carrier density- and temperature-dependent (7–294 K) studies on BSTS films with thicknesses of 22 nm and 192 nm. In the 22 nm film, the two decay constants τ_1 and τ_2 increase with carrier density at room temperature but decrease with temperature at a carrier density of $1.7 \times 10^{19} \text{ cm}^{-3}$. A detailed analysis suggests that τ_1 arises from electron-phonon scattering and carrier diffusion, while τ_2 likely results from defect-assisted and phonon-assisted recombination. Furthermore, increasing the sample temperature leads to anharmonic decay induced softening of $\sim 14\%$ in the phonon frequency and an anomalous $\sim 48\%$ decrease in the phonon damping parameter due to reduced Dirac surface electron and acoustic phonon scattering. Temperature-dependent studies of the 192 nm film reveal a $\sim 7\%$ reduction in sound velocity, in contrast to the 14% reduction observed in the 22 nm film.

I. INTRODUCTION

Topological insulator (TI) thin films have emerged as a fascinating class of materials in condensed matter physics due to their remarkable ability to support conducting surface states while remaining insulating in the bulk [1–3]. These surface states arise from an interplay of spin-orbit coupling and time-reversal symmetry, which induces a band inversion, leading to the crossing of conduction and valence bands at the surface, resulting in symmetry protected gapless Dirac surface states [4, 5]. Many well-known TI materials, such as Bi_2Se_3 and Bi_2Te_3 , suffer from

* nkamaraju@iiserkol.ac.in; Department of Physical Sciences, Indian Institute of Science Education and Research
Kolkata, Mohanpur, 741246, West Bengal, India.

poor bulk insulating properties, limiting the ability to investigate the anticipated novel surface phenomena [5, 6]. In contrast, $\text{BiSbTe}_{1.5}\text{Se}_{1.5}$ (BSTS) has emerged as the promising TI material displaying robust insulating bulk states [7–9], making it ideal for exploring the exotic Dirac surface states. BSTS demonstrates higher surface conductivity [1, 10] and lower thermal conductivity [12] compared to Bi_2Se_3 , Bi_2Te_3 , and $\text{Bi}_2\text{Te}_2\text{Se}$, making it an attractive candidate for applications in quantum computing [13, 14], spintronics [15, 16], and thermoelectrics [10, 17–19].

Ultrafast studies are essential for advancing thermoelectric devices, as they provide critical insights into the fundamental processes governing charge and heat transport on ultrafast timescales. These ultrafast pump-probe studies have been utilised to infer the non-equilibrium surface and bulk electron, and phonon dynamics, which are crucial for optimizing thermoelectric materials [5, 9, 15, 22, 25, 26]. In these experiments, upon irradiation of a femtosecond pump pulse on a material, acoustic phonons along with the photoexcited carriers are generated. A time delayed probe pulse is then used for detection, which gets reflected from the top surface of the material and also from the travelling acoustic phonons. This in turn results in the interference between these two reflections at the detector, revealing rich information about the acoustic phonons in the material. The mechanism for the generation of these acoustic phonons can involve the contribution of thermo-elastic stress [5, 6, 28] and deformation potential stress [5, 6, 28–30] in semiconductors.

The propagation of these acoustic phonons in thin films depends on different factors like the thickness of the film, excited carrier density and sample temperature. For instance, if the thickness of the sample is much more than the penetration depth (ξ), it can host travelling acoustic strain pulses (TASP) [5, 25]. Conversely, when the thickness is less than the penetration depth, the film can act as an acoustic phonon resonator (APR) [31]. To the best of our knowledge, there is no comprehensive investigation of how the TASP emerges from the CAPs. Thus, investigating the photoexcited carriers and propagation of acoustic phonons in BSTS thin films is expected to provide valuable insights, which are essential for understanding thermal transport in TI-based thermoelectric devices. In this regard, it is important to inspect if there is any coupling between the acoustic phonons and the surface electrons as the energy of the acoustic phonons is comparable to surface electrons near the Dirac point.

In this study, we have presented an extensive investigation of the carrier and CAP dynamics in BSTS thin films of various thicknesses, as a function of carrier density and temperature, using degenerate pump-probe reflection spectroscopy. The time-resolved reflectivity signal reveals the presence of acoustic strain pulses, along with an exponentially decaying response from the excited

carriers. The BSTS-Sapphire interface is found to have the best acoustic strain pulse reflectivity of $\sim 42\%$ in comparison to the interface of BSTS-GaAs, BSTS-Si and BSTS-MgO. Hence, the BSTS thin film with sapphire interface has been selected to study the influence of varying thickness (d) on the transient reflectivity data. Our experiments unveil the interplay between two distinct regimes, where the dynamics of acoustic phonons are predominantly influenced by TASP for higher thickness of the film and APR modes as the film thickness decreases. The transient reflectivity data for the films with $d \gtrsim 2\xi$ mainly contains the TASP on top of a single-exponential electronic background with a decay time constant of ~ 2 ps. These TASPs are simulated by the well-known theoretical acoustic strain model [5, 22]. And the transient reflectivity data for BSTS films with $d < \xi$ is dominated by APR modes and a bi-exponential electronic background. To further understand the behaviour of carriers and CAP dynamics, a detailed carrier density and temperature dependent study is carried out on 22 nm and 192 nm thick BSTS films on sapphire. The bi-exponential electronic background for the 22 nm film ($\tau_1 \sim 2$ ps and $\tau_2 \sim 350-450$ ps) and CAP parts display strong dependence on the carrier density and temperature. Both the τ_1 and τ_2 are observed to increase by $\sim 12\%$ and $\sim 20\%$ respectively with the carrier density variation from 0.8×10^{19} - 13.5×10^{19} cm^{-3} . And both τ_1 and τ_2 decrease by $\sim 15\%$ and $\sim 12\%$ respectively as the sample is heated from 7-294 K. A detailed analysis of τ_1 and τ_2 as functions of carrier density (at room temperature) and temperature (at constant carrier density) reveals that τ_1 arises from the interplay between electron-phonon scattering and carrier diffusion, while τ_2 is likely to originate from the combined effects of defect-assisted and phonon-assisted recombination. The acoustic phonon lifetime and frequency for the 22 nm film, decreases with increasing carrier density, suggesting an enhancement in electron-phonon scattering. The acoustic phonon frequency softens by $\sim 14\%$ with increasing temperature, in line with normal behavior, while the phonon damping factor shows an anomalous decrease as the temperature rises due to decreased scattering between the Dirac surface electrons and acoustic phonons. Temperature-dependent studies reveal a $\sim 7\%$ reduction in sound velocity for the 192 nm film, in contrast to $\sim 14\%$ reduction observed in the 22 nm film as the sample temperature is increased.

II. METHODS

BSTS crystallizes in a rhombohedral structure with $R\bar{3}m$ space-group symmetry. In this work, pulsed laser deposition (PLD) technique has been utilised to deposit all BSTS thin films on various

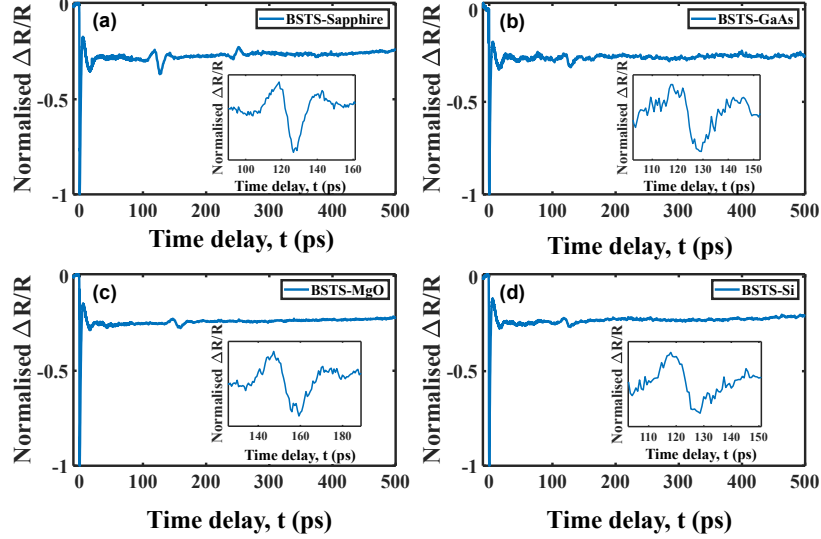


FIG. 1. Time-resolved normalised $\Delta R/R$ signal as a function of time delay between the pump and probe showing acoustic strain pulses on the top of exponentially decaying electronic background observed for (a) BSTS ($164.9 \text{ nm} \pm 2.5 \text{ nm}$) - Sapphire interface, (b) BSTS ($170.5 \text{ nm} \pm 2.6 \text{ nm}$) - GaAs interface, (c) BSTS ($211.0 \text{ nm} \pm 3.1 \text{ nm}$) - MgO interface and (d) BSTS ($168.7 \text{ nm} \pm 2.6 \text{ nm}$) - Si interface respectively. Inset in each figure shows the enlarged view of first echo of the acoustic strain pulse. Here, the pump and probe fluence are kept constant at $87 \mu\text{J}/\text{cm}^2$ and $6 \mu\text{J}/\text{cm}^2$ respectively.

substrates of sapphire (Al_2O_3), GaAs, MgO and Si. The details of the sample growth procedure using the PLD technique are discussed in the Supplemental Material [32], Sec. I and the details of the substrates are summarized in supplemental material [32], table TS1. The characterization of the thin films using X-ray diffraction (XRD), Raman spectroscopy and scanning electron microscopy (SEM) is discussed in the supplemental material [32], Fig. S1. The thickness of the films is measured using cross-sectional SEM technique (see supplemental material [32], Fig. S2).

The time-resolved reflectivity experiments have been performed using a home-built reflection geometry pump-probe spectroscopy setup (see supplemental [32], Fig. S3). Our setup uses pulsed laser output of an amplifier (RegA 9050, Coherent Inc.) operated at 250 kHz with pulse width of $\sim 60 \text{ fs}$ and central photon energy of $\sim 1.57 \text{ eV}$. The sample temperature is varied using a closed-cycle helium cryostat (OptistatDryBLV, Oxford Instruments). Further details of the pump-probe setup and measurements are provided in the supplemental material [32], sec. II.

For fluence dependent studies, the pump fluence is varied from $11 \mu\text{J}/\text{cm}^2$ to $174 \mu\text{J}/\text{cm}^2$ which corresponds to the carrier density of $\sim 0.8 \times 10^{19} \text{ cm}^{-3}$ to $13.5 \times 10^{19} \text{ cm}^{-3}$. The probe fluence is

kept constant at $6 \mu\text{J}/\text{cm}^2$. The pump fluence is chosen such that the sample remains undamaged. For the analysis, time-resolved $\Delta R/R$ signal is normalised with respect to its peak value.

III. RESULTS AND DISCUSSION

A. Effect of Film thickness on acoustic phonons

The transient reflectivity ($\Delta R/R$) data for BSTS films on four substrates of Sapphire, GaAs, MgO and Si, are shown in Fig. 1(a)-(d). Upon irradiation with the pump pulse, the excitation of non-equilibrium electrons leads to a negative dip ($\Delta R/R$) at zero time delay (see schematic Fig. 6(a)). These photoexcited carriers then undergo carrier-phonon scattering lasting \sim few ps (see schematic Fig. 6(b)) and subsequently undergo interband recombination with the timescales of \sim hundreds of ps as the signal exponentially recovers towards zero [33]. On top of this electronic background, the acoustic strain pulses in the GHz frequency range are observed. These acoustic strain pulses are generated due to the thermo-elastic [5, 22] and deformation potential stress [6] (the theory of generation and detection of acoustic strain pulses is discussed in the supplemental material [32], sec. III). It can be seen from Fig. 1 that, on top of the main acoustic strain pulse, there are also echo pulses that occur due to the multiple reflections of the primary strain pulse.

The calculated values (see supplemental material [32], Table TS3 for details) of acoustic reflection coefficient (r_a) for these pulses is found to be maximum for BSTS-Sapphire interface and minimum for BSTS-Silicon interface as the acoustic strain pulse echoes have maximum amplitude for BSTS-Sapphire interface. In addition, it is seen that the successive echoes are inverted with respect to each other (Fig. 1(a)). This can be understood by considering the boundary conditions at the two interfaces of the film, namely the BSTS-Air and BSTS-Substrate interfaces. At the BSTS-Air interface, a phase shift of ' π ' occurs because the acoustic impedance of air is lower than that of the BSTS film. In contrast, at the BSTS-Substrate interface, no phase shift is observed, as the acoustic impedance of the substrate is higher than that of the BSTS film [5].

Since BSTS-Sapphire interface has the best acoustic reflection coefficient, further time-resolved investigations are carried out on BSTS films of varying thickness on the sapphire substrate. It should be noted here that the effective wavelength of the acoustic strain pulse is $\sim 2\xi$ [5] ($\xi \sim 26$ nm is calculated from UV-visible measurements which is in agreement with the previous literature [9]). The thickness of the BSTS film is thus chosen to be varied from below and above

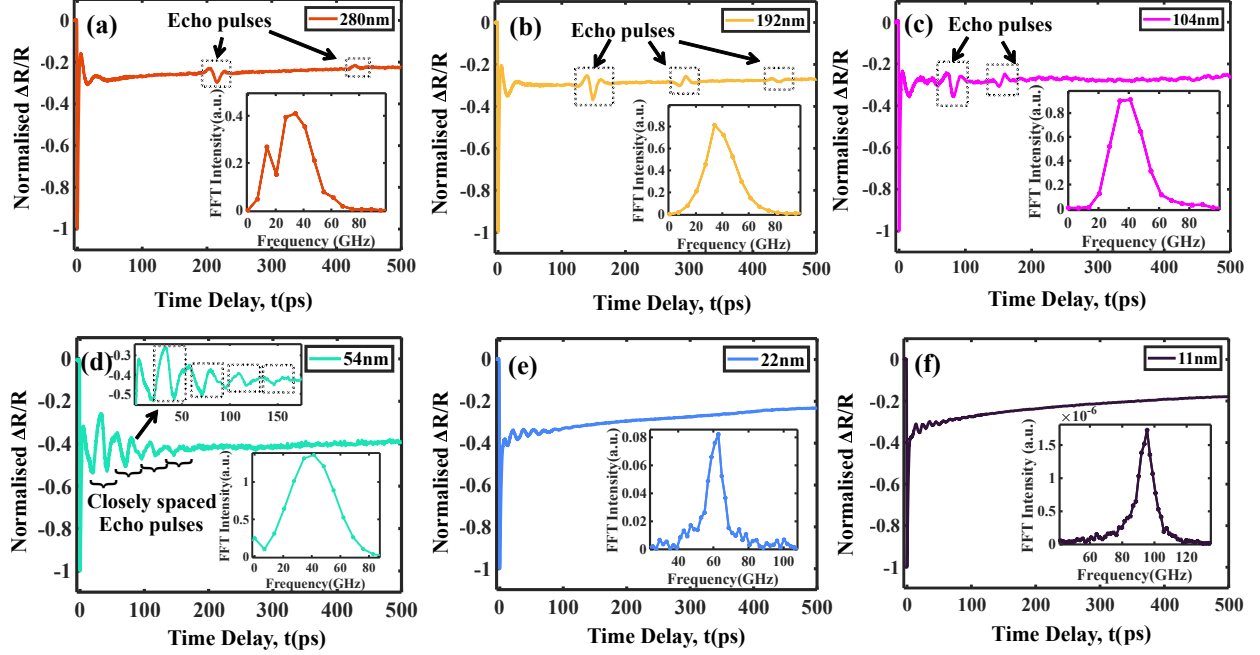


FIG. 2. Time-resolved normalised $\Delta R/R$ signal observed for the different thicknesses of BSTS thin film deposited on Sapphire substrate. (a) BSTS sample of thickness 280 nm shows clearly separated acoustic strain pulses with first and second echo appearing at 215 ps and 428 ps respectively. (b) For 192 nm thick BSTS, the first, second and third echo appears at 148 ps, 295 ps and 442 ps respectively. (c) For 104 nm thick film, first and second echo appears at 81 ps and 160 ps respectively. (d) For 54 nm thick film, four closely spaced echoes, at 32 ps, 71 ps, 109 ps and 146 ps are observed. For (a)-(d) the inset shows the FFT spectra of the extracted first echo of the acoustic strain pulse. (e) The data for the 22 nm thick film displays the oscillatory motion with a period of 16 ps on the top of the bi-exponential decay. Inset shows the FFT of the extracted oscillation peaking at 61 GHz. (f) The data for the 11 nm film shows the oscillatory motion with a period of 10.5 ps in addition to the bi-exponential decay. Inset shows the FFT of the extracted oscillation peaking at 95 GHz. Here, the pump and probe fluence are kept constant at $87 \mu\text{J}/\text{cm}^2$ and $6 \mu\text{J}/\text{cm}^2$ respectively.

the optical penetration depth i.e. from 11 nm to 280 nm. For $d \geq 2\xi$ ($\gtrsim 52$ nm i.e. for 104 nm, 192 nm and 280 nm films), the clearly separated acoustic strain pulses on top of the single-exponential electronic background (~ 2 ps) are observed in the time domain (Fig.2(a)-(d)) with separation $2d/v_s$, where v_s denotes the longitudinal sound velocity. And the Fast Fourier transform (FFT) of the extracted first echo of the acoustic strain pulse (see supplemental material [32], sec. V for details) shows a broad spectrum peaking around 35-40 GHz (insets in Fig. 2(a)-(d)). For the 54

nm film, with $d \sim 2\xi$, the strain echo pulses are very closely spaced (shown in Fig. 2(d)). As the thickness of the film is further reduced (< 52 nm i.e. for 11 nm and 22 nm films), the pump beam penetrates into the substrate completely and the entire film gets excited. Here, we observe clear oscillations in time-domain with narrower FFT intensity spectrum (Fig. 2(e), (f)). This is because a thin film with thickness less than the penetration depth acts as an acoustic phonon cavity whose fundamental resonance frequency is solely determined by its thickness [31]. Thus, only the acoustic phonon whose frequency matches with the fundamental cavity resonance survives, displaying spectral narrowing, and these are referred as APR modes. The relationship between the excited fundamental resonant mode frequency (ν_{LA}) and thickness in thin films is given by, $\nu_{LA} = v_s/2d$. The frequency of the excited modes obtained after subtracting the electronic background (see supplemental [32], sec. V for details) for the 11 nm and 22 nm films is ~ 95 GHz and ~ 61 GHz respectively (shown in the inset of Fig. 2(e), 2(f) respectively). Here, the electronic background is of bi-exponential nature ($\tau_1 \sim 2.0$ - 2.6 ps and $\tau_2 \sim 263$ - 380 ps) and dominant as compared to the data for $d \geq 2\xi$ in the pump probe time delay (see supplemental [32], Fig. S7).

The variation of the acoustic phonon frequency (central frequency of the FFT intensity spectra) with increasing thickness is shown in Fig. 3(a), and is expected to follow the expression $\nu_{LA} = v_s/2d$ [31] (orange line plotted using $v_s = 2650$ m/s). A deviation from this expression is observed for $d > 26$ nm, as these correspond to the central frequencies of the FFT intensity spectrum of TASP, rather than the CAP frequency. Fig. 3(b) shows the variation of the damping time [34] (given by $\frac{1}{\pi * w}$ where "w" is the full width at half maximum of the FFT intensity spectrum) of the acoustic phonons with thickness. Note that the lifetime of the acoustic phonons decreases drastically as we go from APR to TASP regime of thickness due to the formation of the strain pulses.

Taking into account that the origin of the acoustic strain pulses/CAPs in BSTS is linked to the thermo-elastic stress [5, 35] (see supplemental material [32], sec. III for the details of the theory), the complete acoustic strain model proposed by Thomsen et al. [5] has been used to simulate the experimental data. Fig 4. shows the experimental and simulated data for 54 nm (see Fig. 4(a)-(b)), 104 nm (see Fig. 4(c)-(d)), 192 nm (see Fig. 4(e)-(f)), and 280 nm (see Fig. 4(g)-(h)) films. Here, a clear alignment between theoretical and experimental results is evident.

Now, using the calculated sound velocity of 2650 ± 36 m/s in the BSTS film and the observed period of oscillation (T) for CAPs (for $d < \xi$) or the time separation ($T' = t_2 - t_1$) between the acoustic strain pulses (for $d \gtrsim \xi$), the thickness of the films can be estimated and these values are

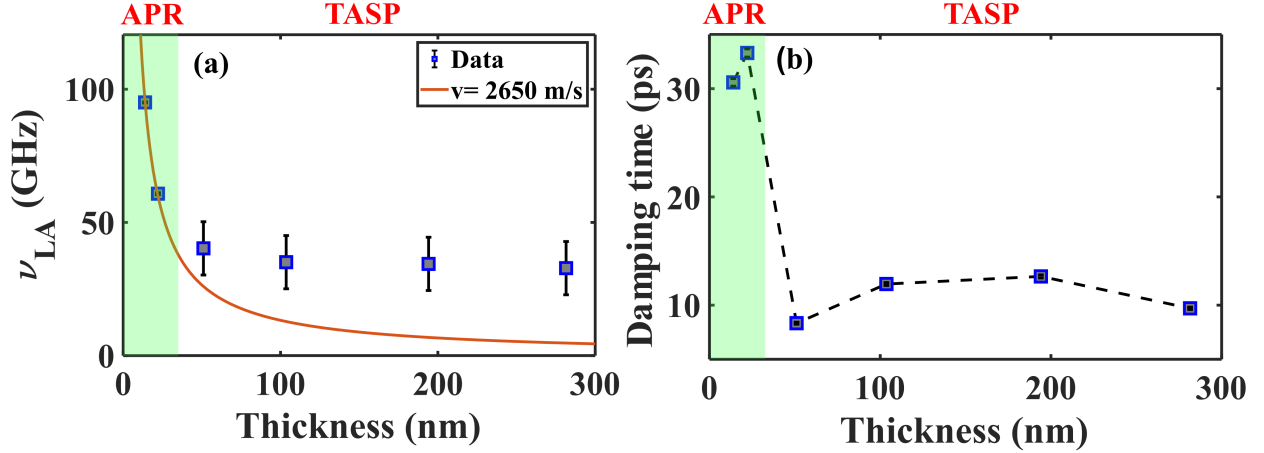


FIG. 3. (a) The variation of central frequency of FFT intensity for the CAPs as a function of thickness. Orange solid line shows the plot with $\nu_{LA} = 2d/v_s$ where $v_s = 2650$ m/s. (b) The damping time ($\frac{1}{\pi * w}$, where "w" is the full width at half maximum of the FFT intensity spectrum) of the CAPs with increasing thickness. Here, the data are represented by blue open squares and dotted lines are guide to the eye.

TABLE I. Estimated thickness and measured thickness (from cross-sectional SEM) of all the films

Period of Osc. T (ps)	Est. Thickness $d = v_s T/2$ (nm)	Measured thickness from cross-sectional SEM (nm)
10.5 ± 0.2	13.9 ± 0.5	11.4 ± 2.0
16.6 ± 0.2	22.1 ± 0.6	22.5 ± 2.0
Time sep. b/w echoes $T' = \tau_2 - \tau_1$ (ps)	Est. Thickness $d = v_s T'/2$ (nm)	Measured thickness from cross-sectional SEM (nm)
38.5 ± 0.2	51.0 ± 0.6	53.9 ± 2.0
78.2 ± 0.2	103.6 ± 1.7	104.3 ± 2.0
146.5 ± 0.2	194.1 ± 2.9	191.9 ± 2.0
212.4 ± 0.2	281.5 ± 4.1	280.2 ± 2.0

found to be in close agreement with the thickness measured from cross-sectional SEM (see Table I and the supplemental material [32], Fig. S2).

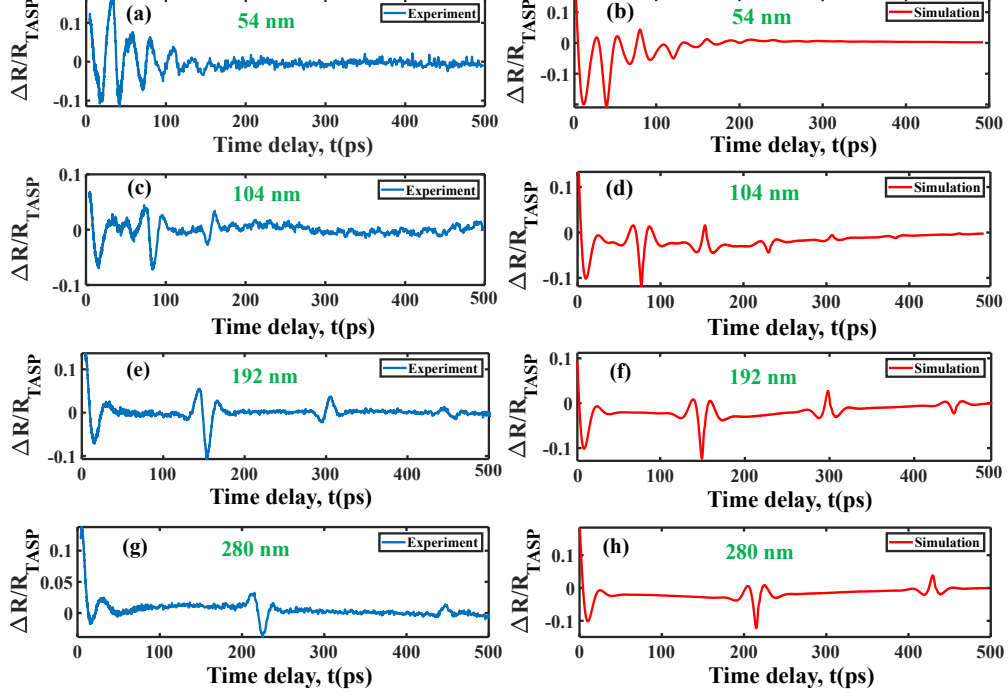


FIG. 4. Simulation of the acoustic strain pulses using Thomsen model ([5, 6]). Blue curves (a), (c), (e) and (g) are the extracted $\Delta R/R_{TASP}$ signal for the 54 nm, 104 nm, 192 nm and 280 nm BSTS film respectively. And red curves (b), (d), (f) and (h) are the simulations using the Thomsen model ([5, 6]) for the 54 nm, 104 nm, 192 nm and 280 nm BSTS film respectively.

B. Effect of photoexcited carriers on CAPs and strain dynamics

As the electron and CAPs dynamics are more prominent for $d < \xi$, we selected the BSTS sample with $d = 22$ nm for further investigation by varying the carrier density at room temperature (see Fig. 5(a)). The $\Delta R/R$ data show an oscillatory pattern due to the CAPs on top of the bi-exponential electronic background. The data could be well fitted (for \mathcal{R}^2 values, see supplemental material [32], Table TS5) with the following function,

$$\frac{\Delta R}{R} = \left[\left\{ A_0 + \sum_{i=1}^2 A_i e^{-t/\tau_i} + B_{LA} e^{-t/\tau_{LA}} \cos(2\pi\nu_{LA}t + \phi_{LA}) \right\} \times (1 - e^{-t/\tau_r}) \right] \otimes CC(t) \quad (1)$$

where the multiplication factor, $(1 - e^{-t/\tau_r})$ of eq. (1) represents the initial rise of the $\Delta R/R$ signal giving a rise time, $\tau_r \sim 255$ fs, that corresponds to the thermalisation of excited carriers [33]. $CC(t)$ here is the pump-probe cross correlation function with FWHM of ~ 235 fs. The first term

inside the parenthesis, A_0 represents amplitude of the long-lived carrier recombination dynamics. The second term in the parenthesis of eq. (1) signifies the bi-exponential electronic background (A_1, A_2 and τ_1, τ_2 are the decay coefficients and the decay time constants of the excited carriers respectively). Finally, the third term of the eq. (1) inside the parenthesis, is the damped harmonic oscillator function for the CAPs ($B_{LA}, \tau_{LA}, \nu_{LA}$ and ϕ_{LA} are the amplitude, lifetime, frequency and phase of the CAPs).

The behaviour of the decay time constants at various carrier densities is shown in Fig. 5(b)-(c). We observe that A_1 contributes dominantly $\sim 70-78\%$ of the decay process whereas A_0 and A_2 contributes around $\sim 12-14\%$ and $\sim 11-15\%$ respectively (see supplemental material [32], Fig. S9 for details). The decay time constants, $\tau_1 \sim 2$ ps and $\tau_2 \sim 340-410$ ps, increase by $\sim 12\%$ and $\sim 20\%$ respectively, with the carrier density variation from $\sim 0.8 \times 10^{19} \text{ cm}^{-3}$ to $13.5 \times 10^{19} \text{ cm}^{-3}$. The fast decay constant τ_1 , can arise from the thermalisation of carriers via electron-phonon scattering [9, 36, 37] and diffusion of the carriers [34, 38, 39] (see schematic Fig. 6(b)). To understand the observed behaviour of τ_1 with carrier density, we attempted to fit the data with two-temperature model (TTM) [20, 37] but found that it did not provide a satisfactory fit. However, a modified version of the TTM is able to capture the trend of τ_1 with carrier density (for more details, refer to supplemental material [32], sec. VI). Additionally, previous studies [34, 38] on tellurium and Bi_2Te_3 show that carrier diffusion occurs within $\sim 1-2$ ps in topological insulators. Thus, by using the diffusion length of 26 nm ($\sim \xi$) and the observed decay time τ_1 , here in this study, the diffusion constant, D is estimated to be $\sim 2.2 \text{ cm}^2/\text{s}$, that is of the similar order as observed in Bi_2Se_3 [12, 36] at 300 K ($D = 1.2 \text{ cm}^2/\text{s}$). This implies that both electron-phonon scattering and diffusion of carriers are plausibly contributing to the decay time constant τ_1 . The slow decay time constant τ_2 is increasing with the carrier density by $\sim 20\%$ (340-410 ps). Such a behaviour indicates that τ_2 likely originates from the defect-assisted recombination as the BSTS thin films are known to host Bi, Sb anti-site defects and Se vacancy defects [42] (see schematic Fig. 6(c)). The observed behaviour for τ_2 can be explained as follows: as the carrier density increases, the number of available defect states reduces. This reduction leads to a delay in the ability of new carriers to occupy the available defect states, thereby increasing τ_2 with rise in carrier density.

Next, we turn our attention to the variation of amplitude (B_{LA}), damping parameter (Γ_{LA}) and frequency (ν_{LA}) of CAPs (see Fig. 5(d)-(e)). The amplitude of the phonon, B_{LA} (see supplemental material [32], Fig. S9(c)), initially increases and then saturates at higher carrier density (which is also seen in bulk CdSe [43]). The observed increase in B_{LA} with carrier density further cor-

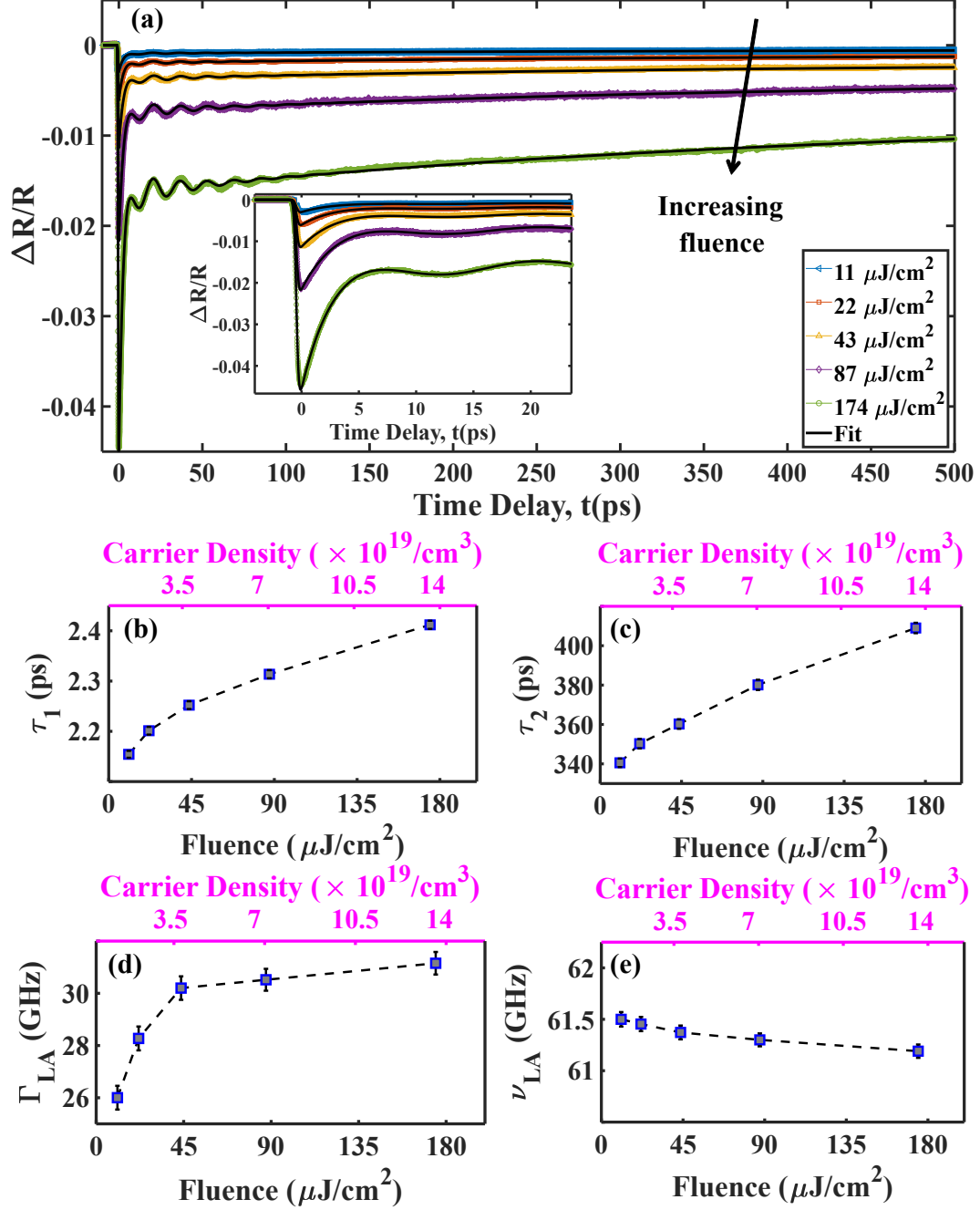


FIG. 5. (a) The time-resolved $\Delta R/R$ signal at various pump fluences from 11 $\mu\text{J}/\text{cm}^2$ to 174 $\mu\text{J}/\text{cm}^2$ (different colour symbols shows different fluences) for 22 nm BSTS film at room temperature and black solid line shows the fit using eq. (1). The direction of the arrow indicates that the pump fluence is increasing from top curve to the bottom curve. (b) and (c) display the variation of τ_1 and τ_2 respectively. (d) and (e) show the behaviour of phonon damping parameter Γ_{LA} ($1/\tau_{LA}$) and frequency, ν_{LA} of the CAP respectively. Here, the data are represented by blue open squares and dotted lines are guide to the eye.

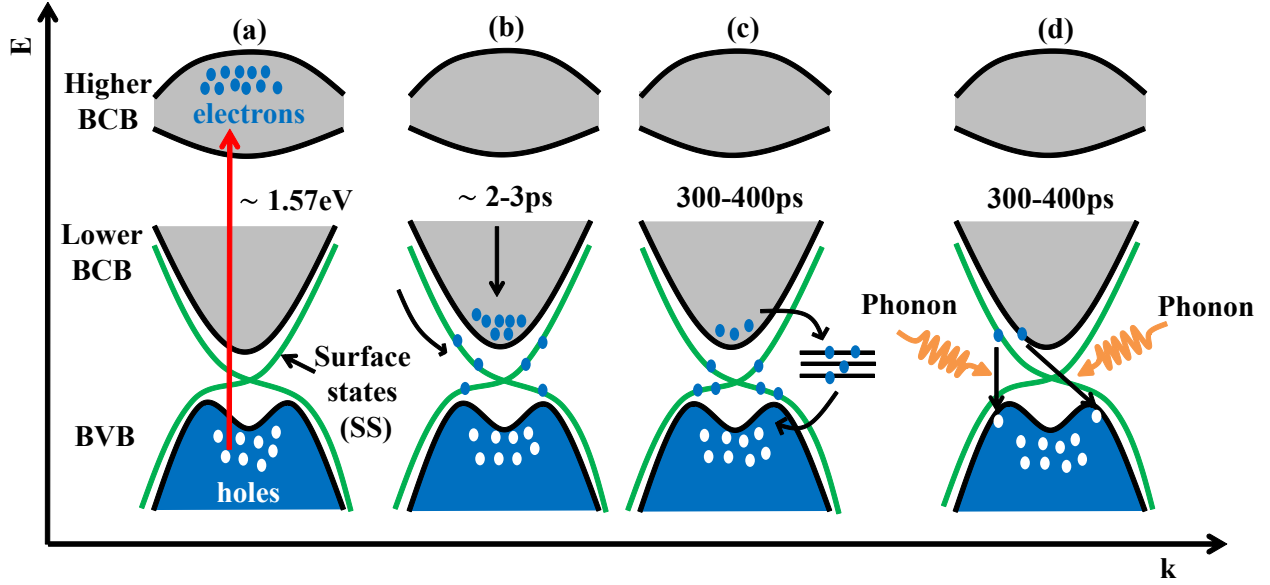


FIG. 6. Schematic for the various processes in BSTS. (a) The initial excitation of the electrons upon irradiation with the pump pulse from bulk valence band (BVB) to higher conduction band (BCB). (b) The relaxation of electrons towards the lower BCB edge through electron-phonon scattering and diffusion of carriers. (c) The recombination of electrons and holes via defect states. (d) The recombination process of surface or bulk electrons and holes via phonons.

robbrates that the generation of CAPs is resulting from thermo-elastic and deformation potential stresses [5, 43]. An increase in carrier density induces greater strain at the surface, which in turn leads to a higher amplitude of the generated phonons. And the saturation of the B_{LA} at high carrier densities may be attributed to an increase in the optical band gap resulting in the saturation of absorption due to the Burstein-Moss effect [44, 45]. Subsequently, the Γ_{LA} ($1/\tau_{LA}$) of CAPs increases by $\sim 19\%$ with increase in carrier density (see Fig. 5(d)). This is attributed to the increased scattering interactions between electrons and phonons, which in turn reduces the phonon lifetime. Further, the frequency of the CAPs remains nearly constant with increase in carrier density (see Fig. 5(e)). This can be understood as follows: The CAPs are generated near the surface of the BSTS film, but they rapidly propagate away from the region of carrier excitation. The penetration depth in the BSTS film is about 26 nm, with the CAPs traversing this thickness in only 9 ps, a time shorter than the single oscillation period (~ 16 ps). Consequently, the impact of pump fluence on the CAPs' frequency is very less (which is also seen in bulk CdSe [43]). Our photoexcited carrier density dependent studies on 192 nm thick samples do not show interesting features except for the monotonic linear increase in its TASP amplitude with increase in the carrier density (data not

shown).

C. Effect of temperature on carriers and CAPs dynamics

To understand the carrier and CAPs dynamics in BSTS further, temperature-dependent investigations were carried out from 7-294 K at fixed carrier density of $1.7 \times 10^{19} \text{ cm}^{-3}$ on 22 nm and 192 nm BSTS films. Fig. 7(a) shows the time-resolved $\Delta R/R$ signal for 22 nm BSTS film at various temperatures. The data is fitted with eq.(1) (black solid line in Fig. 7(a)) and the parameters obtained are shown in Fig. 7(b)-(e). We observe that A_0 , A_1 and A_2 contribute around $\sim 8-16 \%$, $\sim 70-75 \%$ and $\sim 12-20 \%$ respectively in the whole temperature range (see supplemental material [32], Fig. S10). The decay time constants τ_1 and τ_2 , decrease by $\sim 15 \%$ and $\sim 12 \%$ respectively in the measured temperature range (see Fig. 7(b)-(c)). The behaviour of τ_1 versus temperature also corroborates our earlier attribution of this constant to an interplay of electron-phonon scattering and diffusion of carriers as seen in similar narrow band-gap semi-metal Te [34]. After thermalisation between electrons and phonons, electrons can accumulate near the conduction band minima and subsequently recombine with the holes near the valence band maxima. Since the direct recombination process is of the order of \sim nanoseconds [33], it cannot explain the observed temperature-dependent behaviour of τ_2 . However, phonon-assisted electron-hole recombination, in which an electron and a hole recombine through a phonon, can account for τ_2 . Previous time-resolved studies on semimetals and topological materials like Bi [46], WTe₂ [47], NiTe₂ [48] and MnBi₂Te₄ [49] have demonstrated that the phonon-assisted electron-hole recombination (see schematic Fig. 6(d)) time exhibits a significant dependence on temperature, as the phonon population is strongly temperature-dependent. At low temperatures, the electron-hole recombination time is longer due to the reduced efficiency of interband electron-phonon scattering, and a similar behaviour is experimentally observed in τ_2 (see Fig. 7(c)). In addition, the electronic structure of the BSTS allows for the possibility of flat band bending [50, 51], which favors this indirect recombination. Thus, we attribute the τ_2 process to phonon-assisted electron-hole recombination, which can be quantitatively described by [46]:

$$\frac{1}{\tau_2} = \mathcal{B} \frac{q}{\sinh^2 q} + \frac{1}{\tau_{20}} \quad (2)$$

where $q = \hbar\omega_r/2k_B\bar{T}$ and ω_r is the frequency of the phonon participating in the electron-hole recombination, \hbar is the reduced Planck's constant, k_B is the Boltzmann constant and \bar{T} is the

temperature. τ_{20} is the temperature-independent term that is influenced by defects or impurities in the sample. The parameter " \mathcal{B} " signifies the density of states in the energy bands of electrons and matrix elements that govern interband scattering between electrons and holes. Fig. 7(c) shows the data and the fit with $\omega_r/2\pi = 2.00$ THz (A_{1g}^1 Raman mode) and $\tau_{20} \sim 404$ ps (pink line); $\omega_r/2\pi = 0.07$ THz (acoustic phonon mode) and $\tau_{20} \sim 406$ ps (cyan line). This model yields temperature-independent $\tau_{20} \sim 404$ -406 ps, which is only due to impurities/defects at the lowest temperature. From our fit, it is clear that both the acoustic and optical phonons may be involved in the phonon-assisted recombination process. Thus, the decay time constant τ_2 can be defined as: $\frac{1}{\tau_2} = \frac{1}{\tau_d} + \frac{1}{\tau_{ph}}$. Here, τ_2 captures an effective electron-hole recombination decay channel consisting of two parallel decay processes through defects (τ_d) and phonons (τ_{ph}). In the carrier density-dependent study at room temperature, the lattice temperature remains relatively constant within ~ 5 K, indicating dominant defect-assisted recombination with a possible contribution from the phonon-assisted recombination process as well. However, from temperature-dependent studies, we find strong dependence of τ_2 on the sample temperature down to 7 K indicating dominant phonon-assisted recombination process.

The temperature dependence of the CAP damping parameter and frequency are shown in Figs. 7(d) and 7(e), which suggests phonon softening with increasing temperature. The frequency of the CAP decreases from ~ 71 GHz to ~ 61 GHz which is nearly 14 % as the sample is heated from 7-294 K. And the damping parameter ($\Gamma_{LA} = 1/\tau_{LA}$) of the phonon decreases by 48 % from ~ 54 GHz at 7 K to ~ 28 GHz at 294K exhibiting a rather anomalous behaviour similar to previously observed for CAPs in BSTS single crystal [9]. The temperature dependence of the phonon mode frequency [34, 52–55] can be described as: $\nu_{LA}(\bar{T}) = \nu_0 + \Delta\nu_{anh}(\bar{T})$ where the first term ν_0 is the frequency of the phonon at absolute zero temperature. The second term accounts for the intrinsic anharmonic contribution to phonon frequency from the decay of a phonon into two phonons (cubic anharmonicity) or three phonons (quartic anharmonicity), originating from the real part of the phonon self-energy [34, 52–55]. Taking into account only cubic phonon-phonon anharmonic interactions, the change in frequency is given by : $\Delta\nu_{anh}(\bar{T}) = A \left[1 + \frac{2}{\exp(\frac{h\nu_0}{2k_B\bar{T}}) - 1} \right]$. Here, h is the Planck's constant, k_B is the Boltzmann constant, \bar{T} is the temperature and A is the cubic anharmonicity-induced self-energy parameter, which is negative for normal redshift. The solid red line in Fig. 7(e) is the fit using the anharmonic decay model and the parameters obtained after fitting are: $\nu_0 = 73.348 \pm 0.595$ GHz, $A = -0.030 \pm 0.003$ GHz. The temperature-dependent

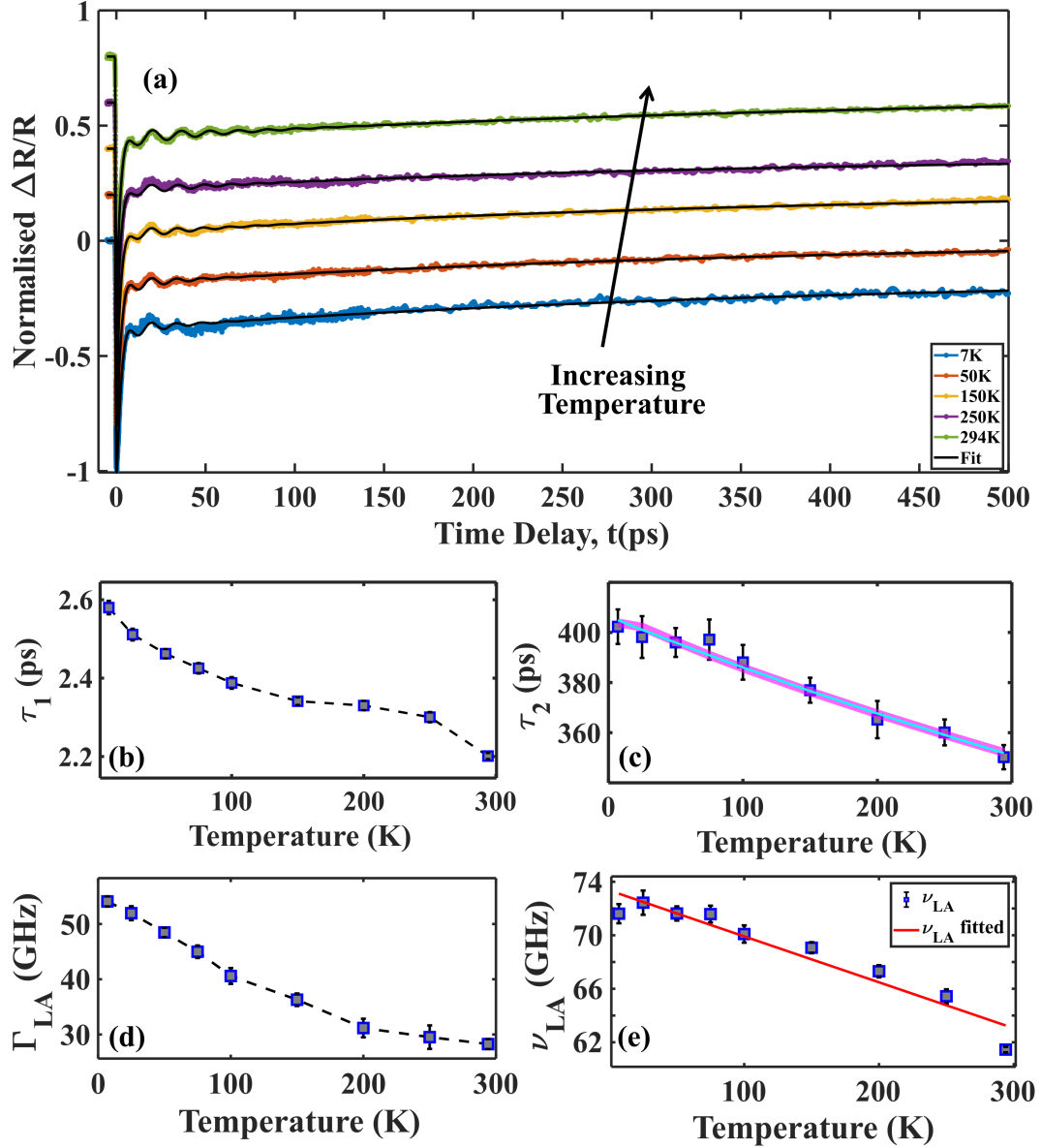


FIG. 7. (a) The normalised time-resolved $\Delta R/R$ signal for 22 nm BSTS film at various temperatures and black solid line shows the fit. The data has been shifted vertically for clarity. (b) and (c) display the variation of τ_1 and τ_2 for the carriers with temperature from 7-294 K respectively. Pink and cyan line in (c) are the fit using phonon-assisted recombination model (eq. (2)) with $\omega_r/2\pi = 2.0$ THz and 0.073 THz respectively. (d) and (e) display the variation of the damping parameter ($\Gamma_{LA} = 1/\tau_{LA}$) and frequency (ν_{LA}) of the CAPs respectively with temperature from 7-294 K. Red solid curve is the fit using anharmonic decay model. Here, the data are represented by blue open squares and dotted lines are guide to the eye.

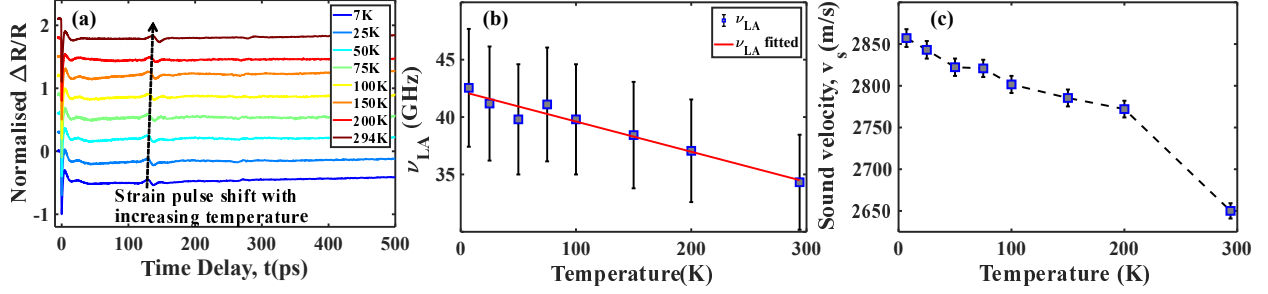


FIG. 8. (a) The normalised time-resolved $\Delta R/R$ signal for 192 nm BSTS film at various temperatures. The data has been shifted vertically for clarity. (b) The variation of the central frequency of the strain pulse as a function of temperature. Red solid curve is the fit using anharmonic decay model. (c) The behaviour of sound velocity with increase in temperature. Here, the data are represented by blue open squares and dotted lines are guide to the eye.

decay of the CAP can proceed through two pathways: a phonon either decays into two phonons via cubic anharmonicity effect or, in the presence of strong electron-phonon coupling (EPC), it decays by generating an electron-hole pair [56, 57]. The damping parameter of the CAP for cubic anharmonicity effect will increase with rising temperature in contrast to the observed behaviour of Γ_{LA} here (see Fig. 7(d)). This discrepancy suggests that the EPC process should be taken into account, which is sensitive to the zero temperature joint electron-hole pair density of states at phonon energy [57]. At low temperatures, the surface electrons near Dirac point can contribute significantly to EPC than at room temperature where thermal excitations reduce the available surface electronic states for transition [57]. Thus, our studies here indicate that EPC plays a crucial role in the acoustic phonon decay in BSTS.

For the 192 nm BSTS (as shown in Fig. 8), we observed similar softening in the central frequency of the acoustic phonon spectrum as a function of temperature. Fig. 8(a) displays the time-resolved $\Delta R/R$ signal over the temperature range of 7 K to 294 K. Fig. 8(b) illustrates the redshift in the frequency with increasing temperature and the solid red curve represents the fit using the cubic anharmonicity model, with the following fit parameters: $\nu_0 = 42.246 \pm 0.360$ GHz, $A = -0.013 \pm 0.001$ GHz. As the temporal separation between the first and second echoes of the strain pulse increases with temperature, one can estimate the variation of the sound velocity ($v_s = 2d/T'$) as a function of temperature (see Fig. 8 (c)). We observe $\sim 14\%$ and $\sim 7\%$ reduction in sound velocity for 22 nm [58] and 192 nm film respectively as the sample temperature rises from 7 K to 294 K. The anomalous behaviour of the acoustic phonon damping parameter in our work

here on 22 nm BSTS films requires further investigation using other techniques such as Brillouin scattering as well as comprehensive theoretical analysis. We believe that the experimental finding here will contribute in designing improved thermoelectric devices based on BSTS.

IV. CONCLUSION

In conclusion, we have employed degenerate pump-probe reflection spectroscopy to study ultrafast carrier dynamics, coherent acoustic phonons, and acoustic strain pulses in BSTS topological insulator thin films of varying thicknesses. We have selected sapphire as the substrate due to its high acoustic reflection coefficient. For films with thickness $d \gtrsim 2\xi$, transient reflectivity data reveals travelling strain pulses with a single-exponential background, while for $d < \xi$, the response is dominated by CAPs and a bi-exponential electronic background with time constants $\tau_1 \sim 2$ ps and $\tau_2 \sim 260$ -380 ps. The strain pulse dynamics are well-described by a theoretical acoustic strain model. To further understand the physics governing photo-excited carrier, CAPs, and strain pulse dynamics, we have performed carrier density and temperature-dependent studies (7–294 K) on 22 nm and 192 nm BSTS films. The fast decay time constant (~ 2 ps) is attributed to electron-phonon scattering and carrier diffusion, while the slower decay time constant (~ 340 -410 ps) is linked to defect- and phonon-assisted recombination. In the 22 nm film, CAP frequency softened with increasing temperature due to cubic anharmonicity, while the damping parameter anomalously decreased, due to acoustic phonon scattering with Dirac surface electrons. Temperature-dependent studies reveal a reduction in sound velocity with rising temperature in both 22 nm and 192 nm films. These findings provide insights into the interplay of electronic and acoustic dynamics in BSTS, offering valuable guidance for designing advanced thermoelectric devices and motivating further theoretical and experimental investigations.

ACKNOWLEDGMENTS

The authors thank the Ministry of Education (MoE), Government of India, for funding and IISER Kolkata for the infrastructural support to carry out the research. The authors thank Prof. Debansu Chaudhuri and Debjit Biswas for the UV-Visible measurements. Anupama, Sidhanta Sahu, Poulami Ghosh, Dheerendra Singh and Sambhu G Nath thank CSIR, UGC, DST-INSPIRE,

IISER Kolkata and UGC for the research fellowship, respectively.

- [1] C. L. Kane and E. J. Mele, A new spin on the insulating state, *Science* **314**, 1692 (2006).
- [2] J. Moore, The next generation, *Nature Physics* **5**, 378 (2009).
- [3] J. E. Moore, The birth of topological insulators, *Nature* **464**, 194 (2010).
- [4] P. Roushan, J. Seo, C. Parker, and Y. Hor, D. Hsieh, D. Qian, A. Richardella, MZ Hasan, RJ Cava, and A. Yazdani, Topological surface states protected from backscattering by chiral spin texture, *Nature (London)* **460**, 1106 (2009).
- [5] M. Z. Hasan and C. L. Kane, Colloquium: Topological insulators, *Reviews of modern physics* **82**, 3045 (2010).
- [6] D.X. Qu, Y. S. Hor, J. Xiong, R. J. Cava, and N. P. Ong, Quantum oscillations and hall anomaly of surface states in the topological insulator Bi_2Te_3 , *Science* **329**, 821 (2010).
- [7] P. Di Pietro, F. M. Vitucci, D. Nicoletti, L. Baldassarre, P. Calvani, R. Cava, Y. S. Hor, U. Schade, and S. Lupi, Optical conductivity of bismuth-based topological insulators, *Physical Review B—Condensed Matter and Materials Physics* **86**, 045439 (2012).
- [8] S. Singh, R. Gopal, J. Sarkar, A. Pandey, B. G. Patel, and C. Mitra, Linear magnetoresistance and surface to bulk coupling in topological insulator thin films, *Journal of Physics: Condensed Matter* **29**, 505601 (2017).
- [9] R. K. Gopal, S. Singh, A. Mandal, J. Sarkar, and C. Mitra, Topological delocalization and tuning of surface channel separation in $\text{Bi}_2\text{Se}_2\text{Te}$ topological insulator thin films, *Scientific Reports* **7**, 4924 (2017).
- [10] A. Taskin, Z. Ren, S. Sasaki, K. Segawa, and Y. Ando, Observation of dirac holes and electrons in a topological insulator, *Physical Review Letters* **107**, 016801 (2011).
- [11] B. Xia, P. Ren, A. Sulaev, P. Liu, S.Q. Shen, and L. Wang, Indications of surface-dominated transport in single crystalline nanoflake devices of topological insulator $\text{Bi}_{1.5}\text{Sb}_{0.5}\text{Te}_{1.8}\text{Se}_{1.2}$, *Physical Review B—Condensed Matter and Materials Physics* **87**, 085442 (2013).
- [12] R. Pathak, P. Dutta, A. Srivastava, D. Rawat, R. K. Gopal, A. K. Singh, A. Soni, and K. Biswas, Strong anharmonicity-induced low thermal conductivity and high n-type mobility in the topological insulator $\text{Bi}_{1.1}\text{Sb}_{0.9}\text{Te}_2\text{S}$, *Angewandte Chemie International Edition* **61**, 41 (2022).

- [13] S. D. Sarma, M. Freedman, and C. Nayak, Majorana zero modes and topological quantum computation, *npj Quantum Information* **1**, 1 (2015).
- [14] A. Y. Kitaev, Fault-tolerant quantum computation by anyons, *Annals of physics* **303**, 2 (2003).
- [15] M. Jamali, J. S. Lee, J. S. Jeong, F. Mahfouzi, Y. Lv, Z. Zhao, B. K. Nikolic, K. A. Mkhoyan, N. Samarth, and J.-P. Wang, Giant spin pumping and inverse spin hall effect in the presence of surface and bulk spin-orbit coupling of topological insulator Bi_2Se_3 , *Nano letters* **15**, 7126 (2015).
- [16] K. Kondou, R. Yoshimi, A. Tsukazaki, Y. Fukuma, J. Matsuno, K. Takahashi, M. Kawasaki, Y. Tokura, and Y. Otani, Fermi level-dependent charge-to-spin current conversion by dirac surface states of topological insulators, *Nature Physics* **12**, 1027 (2016).
- [17] N. Xu, Y. Xu, and J. Zhu, Topological insulators for thermoelectrics, *npj Quantum Materials* **2**, 51 (2017).
- [18] D. Baldomir and D. Faílde, On behind the physics of the thermoelectricity of topological insulators, *Scientific reports* **9**, 6324 (2019).
- [19] M. Tan, Y. Deng, Y. Wang, Z. Zhang, B. Luo, and Z. Lin, Improved performance of thermoelectric micro-device by integrating a layered Bi_2Te_3 film, *Thin solid films* **548**, 526 (2013).
- [20] E. Yapryntseva, O. Ivanov, A. Vasil'ev, and M. Yaprntsev, Microstructure and thermoelectric properties of medium-entropy $\text{BiSbTe}_{1.5}\text{Se}_{1.5}$ and PbSnTeSe compounds prepared by reactive spark plasma sintering, *Semiconductors* **56**, 25 (2022).
- [21] C. Thomsen, H. T. Grahn, H. J. Maris, and J. Tauc, Surface generation and detection of phonons by picosecond light pulses, *Physical Review B* **34**, 4129 (1986).
- [22] C. Thomsen, J. Strait, Z. Vardeny, H. J. Maris, J. Tauc, and J. Hauser, Coherent phonon generation and detection by picosecond light pulses, *Physical review letters* **53**, 989 (1984).
- [23] Y. Wang, C. Liebig, X. Xu, and R. Venkatasubramanian, Acoustic phonon scattering in $\text{Bi}_2\text{Te}_3/\text{Sb}_2\text{Te}_3$ superlattices, *Applied Physics Letters* **97**, 8 (2010).
- [24] L. Cheng, C. Lao Vorakiat, C. S. Tang, S. K. Nair, B. Xia, L. Wang, J.X. Zhu, and E. Chia, Temperature-dependent ultrafast carrier and phonon dynamics of topological insulator $\text{Bi}_{1.5}\text{Sb}_{0.5}\text{Te}_{1.8}\text{Se}_{1.2}$, *Applied Physics Letters* **104**, 21 (2014).
- [25] J. Fonseca, G. M. Diederich, D. Ovchinnikov, J. Yan, D. Xiao, and X. Xu, Picosecond ultrasonics in magnetic topological insulator MnBi_2Te_4 , *Nano Letters* **24**, 34 (2024).
- [26] Y.P. Lai, H.J. Chen, K.H. Wu, and J.M. Liu, Temperature dependent carrier-phonon coupling in topological insulator Bi_2Se_3 , *Applied Physics Letters* **105**, 23 (2014).

- [27] S. Wu, P. Geiser, J. Jun, J. Karpinski, and R. Sobolewski, Femtosecond optical generation and detection of coherent acoustic phonons in GaN single crystals, *Physical Review B—Condensed Matter and Materials Physics* **76**, 085210 (2007).
- [28] P. Ruello, S. Zhang, P. Laffez, B. Perrin, and V. Gusev, Laser induced coherent acoustical phonons mechanisms in the metal insulator transition compound NdNiO₃: Thermal and nonthermal processes, *Physical Review B—Condensed Matter and Materials Physics* **79**, 094303 (2009).
- [29] D. Lim, V. Thorsmølle, R. Averitt, Q. Jia, K. Ahn, M. Graf, S. A. Trugman, and A. J. Taylor, Coherent optical and acoustic phonon generation correlated with the charge-ordering phase transition in La_{1-x}Ca_xMnO₃, *Physical Review B—Condensed Matter and Materials Physics* **71**, 134403 (2005).
- [30] J. Wang, Y. Hashimoto, J. Kono, A. Oiwa, H. MuneKata, G. Sanders, and C. Stanton, Propagating coherent acoustic phonon wave packets in In_xMn_{1-x}As/GaSb, *Physical Review B—Condensed Matter and Materials Physics* **72**, 153311 (2005).
- [31] Y. D. Glinka, S. Babakiray, T. A. Johnson, M. B. Holcomb, and D. Lederman, Acoustic phonon dynamics in thin-films of the topological insulator Bi₂Se₃, *Journal of Applied Physics* **117**, 16 (2015).
- [32] See supplemental material for sample preparation, sample characterization (XRD, Raman spectroscopy and SEM), details of experimental setup, goodness of fit values, and extracted decay amplitudes as a function of fluence and temperature. The Supplemental Material includes Refs. [1–20, 22]].
- [33] G. Prakash, K. Pal, M. Jain, U. Waghmare, and A. Sood, Origin of the thermal expansion anomaly in layered Bi₂Xe₃ topological insulators: Ultrafast time-resolved pump-probe experiments and theory, *Physical Review B* **96**, 075109 (2017).
- [34] N. Kamaraju, S. Kumar, M. Anija, and A. Sood, Large amplitude chirped coherent phonons in tellurium mediated by ultrafast photoexcited carrier diffusion, *Physical Review B—Condensed Matter and Materials Physics* **82**, 195202 (2010).
- [35] M. Hase, P. Fons, A. V. Kolobov, and J. Tominaga, Coherent gigahertz phonons in Ge₂Sb₂Te₅ phase-change materials, *Journal of Physics: Condensed Matter* **27**, 485402 (2015).
- [36] Y. Onishi, Z. Ren, K. Segawa, W. Kaszub, M. Lorenc, Y. Ando, and K. Tanaka, Ultrafast carrier relaxation through auger re combination in the topological insulator Bi_{1.5}Sb_{0.5}Te_{1.7}Se_{1.3}, *Physical Review B* **91**, 085306 (2015).
- [37] J. A. Sobota, S. Yang, J. G. Analytis, Y. Chen, I. R. Fisher, P. S. Kirchmann, and Z. X. Shen, Ultrafast optical excitation of a persistent surface-state population in the topological insulator Bi₂Se₃, *Physical review letters* **108**, 117403 (2012).

- [38] A. Q. Wu, X. Xu, and R. Venkatasubramanian, Ultrafast dynamics of photoexcited coherent phonon in Bi_2Te_3 thin films, *Applied Physics Letters* **92**, 1 (2008).
- [39] C. Zhu, P. Pilch, A. Reinold, D. Kudlacik, G. Springholz, A. Bonanni, M. Assmann, M. Cinchetti, and Z. Wang, Ultra fast dynamics of optically excited charge carriers in the room temperature antiferromagnetic semiconductor $\alpha\text{-MnTe}$, *Phys. Rev. Mater.* **7**, 054601 (2023).
- [40] R. H. Groeneveld, R. Sprik, and A. Lagendijk, Femtosecond spectroscopy of electron-electron and electron-phonon energy relaxation in Ag and Au, *Physical Review B* **51**, 11433 (1995).
- [41] N. Kumar, B. A. Ruzicka, N. Butch, P. Syers, K. Kirshenbaum, J. Paglione, and H. Zhao, Spatially resolved femtosecond pump-probe study of topological insulator Bi_2Se_3 , *Physical Review B—Condensed Matter and Materials Physics* **83**, 235306 (2011).
- [42] A. Pandey, S. Singh, B. Ghosh, S. Manna, R. Gopal, and C. Mitra, Pulsed laser deposition of highly c-axis oriented thin films of BSTS topological insulator, arXiv preprint arXiv:1910.08100 (2019).
- [43] W. Wu and Y. Wang, Ultrafast carrier dynamics and coherent acoustic phonons in bulk CdSe, *Optics Letters* **40**, 64 (2014).
- [44] C. Zhao, S. Cui, Y. Li, Y. Wu, T. Li, K. Li, L. Sun, Z. Sun, C. Xiao, and Y. Xie, Burstein-moss effect leads to an unusual suppression of bipolar conduction with shrinking bandgap, *Journal of Materials Chemistry A* **12**, 23670 (2024).
- [45] A. Dubroka, O. Caha, M. Hronček, P. Friš, M. Orlita, V. Holý, H. Steiner, G. Bauer, G. Springholz, and J. Humlíček, Interband absorption edge in the topological insulators $\text{Bi}_2(\text{Te}_{1-x}\text{Se}_x)_3$, *Physical Review B* **96**, 235202 (2017).
- [46] A. A. Lopez, Electron-hole recombination in bismuth, *Physical Review* **175**, 823 (1968).
- [47] Y. Dai, J. Bowlan, H. Li, H. Miao, S. Wu, W. Kong, P. Richard, Y. Shi, S. A. Trugman, J. X. Zhu, et al., Ultrafast carrier dynamics in the large-magnetoresistance material WTe_2 , *Physical Review B* **92**, 161104 (2015).
- [48] L. Cheng, F. Fei, H. Hu, Y. Dai, F. Song, and J. Qi, Ultrafast carrier and lattice dynamics in the dirac semimetal NiTe_2 , *Physical Review B* **106**, 104308 (2022).
- [49] L. Cheng, T. Xiang, and J. Qi, Magnetic-order-mediated carrier and phonon dynamics in MnBi_2Te_4 , *Physical Review Research* **6**, 023073 (2024).
- [50] S. H. Park, S. Y. Hamh, J. Park, J. S. Kim, and J. S. Lee, Possible flat band bending of the $\text{Bi}_{1.5}\text{Sb}_{0.5}\text{Te}_{1.7}\text{Se}_{1.3}$ crystal cleaved in an ambient air probed by terahertz emission spectroscopy, *Scientific Reports* **6**, 36343 (2016).

- [51] T. Yilmaz, X. Tong, Z. Dai, J. T. Sadowski, E. F. Schwier, K. Shimada, S. Hwang, K. Kisslinger, K. Kaznatcheev, E. Vescovo, et al., Emergent flat band electronic structure in a VSe_2/Bi_2Se_3 heterostructure, *Communications Materials* **2**, 11 (2021).
- [52] A. K. N. M, S. Mukherjee, A. Mukherjee, A. Punjal, S. Purwar, T. Setti, S. P. S, S. Lal, and N. Kamaraju, Probing of magnetic dimensional crossover in $CrSiTe_3$ through picosecond strain pulses (2024), arXiv:2402.01256.
- [53] P. Klemens, Decay of high-frequency longitudinal phonons, *Journal of Applied Physics* **38**, 4573 (1967).
- [54] S. Mukherjee, A. K. NM, S. Manna, S. G. Nath, R. K. Gopal, C. Mitra, and N. Kamaraju, Magnetic order influenced phonon and electron dynamics in $MnBi_2Te_4$ and Sb-doped $MnBi_2Te_4$ investigated by terahertz time-domain spectroscopy, *Physical Review B* **110**, 195401 (2024).
- [55] S. Saha, D. S. Muthu, S. Singh, B. Dkhil, R. Suryanarayanan, G. Dhalenne, H. Poswal, S. Karmakar, S. M. Sharma, A. Revcolevschi, et al., Low-temperature and high pressure raman and x-ray studies of pyrochlore $Tb_2Ti_2O_7$: Phonon anomalies and possible phase transition, *Physical Review B—Condensed Matter and Materials Physics* **79**, 134112 (2009).
- [56] M. Kuiri, S. Das, D. Muthu, A. Das, and A. Sood, Thickness dependent transition from the $1T'$ to Weyl semimetal phase in ultrathin $MoTe_2$: electrical transport, noise and Raman studies, *Nanoscale* **12**, 8371 (2020).
- [57] B. Xu, Y. M. Dai, L. X. Zhao, K. Wang, R. Yang, W. Zhang, J. Y. Liu, H. Xiao, G. Chen, S. A. Trugman, et al., Temperature tunable fano resonance induced by strong coupling between weyl fermions and phonons in TaAs, *Nature communications* **8**, 14933 (2017).
- [58] The reduction in longitudinal sound velocity with increasing temperature is directly proportional to the decrease in the frequency of the coherent acoustic phonon, following the relation: $v_s = 2d v_{LA}$.
- [59] K.B. Han, S. K. Chong, A. O. Oliynyk, A. Nagaoka, S. Petryk, M. A. Scarpulla, V. V. Deshpande, and T. D. Sparks, Enhancement in surface mobility and quantum transport of $Bi_{2-x}Sb_xTe_{3-y}Se_y$ topological insulator by controlling the crystal growth conditions, *Scientific reports* **8**, 17290 (2018).
- [60] N. Kumar, N. Surovtsev, P. Yunin, D. Ishchenko, I. Milekhin, S. Lebedev, A. Lebedev, and O. Tereshchenko, Raman scattering spectroscopy of MBE grown thin film topological insulator $Bi_{2-x}Sb_xTe_{3-y}Se_y$, *Physical Chemistry Chemical Physics* **26**, 13497 (2024).
- [61] R. German, E. V. Komleva, P. Stein, V. G. Mazurenko, Z. Wang, S. V. Streltsov, Y. Ando, and P. H. van Loosdrecht, Phonon mode calculations and raman spectroscopy of the bulk insulating topological

- insulator BiSbTeSe₂, *Physical Review Materials* **3**, 054204 (2019).
- [62] O. B. Wright, B. Perrin, O. Matsuda, and V. Gusev, Ultrafast carrier diffusion in gallium arsenide probed with picosecond acoustic pulses, *Physical Review B* **64**, 081202 (2001).
- [63] M. Fang, Z. Wang, H. Gu, M. Tong, B. Song, X. Xie, T. Zhou, X. Chen, H. Jiang, T. Jiang, and S. Liu, Layer-dependent dielectric permittivity of topological insulator Bi₂Se₃ thin films, *Applied Surface Science* **509**, 144822 (2020).
- [64] I. T. Witting, T. C. Chasapis, F. Ricci, M. Peters, N. A. Heinz, G. Hautier, and G. J. Snyder, The thermoelectric properties of bismuth telluride, *Advanced Electronic Materials* **5**, 1800904 (2019).
- [65] S. V. Ovsyannikov, V. V. Shchennikov, G. V. Vorontsov, A. Y. Manakov, A. Y. Likhacheva, and V. A. Kulbachinskii, Giant improvement of thermoelectric power factor of Bi₂Te₃ under pressure, *Journal of Applied Physics* **104**, 5 (2008).
- [66] X. Chen, H. Zhou, A. Kiswandhi, I. Miotkowski, Y. Chen, P. Sharma, A. Lima Sharma, M. Hekmaty, D. Smirnov, and Z. Jiang, Thermal expansion coefficients of Bi₂Se₃ and Sb₂Te₃ crystals from 10K to 270K, *Applied Physics Letters* **99**, 26 (2011).
- [67] N. Stanton and A. Kent, Propagation of high amplitude strain pulses in sapphire, *Physical Review B—Condensed Matter and Materials Physics* **73**, 220301 (2006).
- [68] M. Kuok, S. Ng, V. Zhang, and D. Lockwood, Acoustic mode dispersion at hypersonic frequencies in GaAs, *Solid state communications* **116**, 27 (2000).
- [69] X. Zhang, C. Li, F. Xu, J. Zhang, C. Gao, Z. Cheng, Y. Wu, X. Liu, A. Zerr, and H. Huang, Sound velocity anisotropy and single-crystal elastic moduli of MgO to 43 GPa, *Journal of Geophysical Research: Solid Earth* **128**, 6 (2023).
- [70] I. Leibacher, S. Schatzer, and J. Dual, Impedance matched channel walls in acoustofluidic systems, *Lab on a Chip* **14**, 463 (2014).

Supplemental Material

I. SAMPLE PREPARATION AND CHARACTERISATION:

BiSbTe_{1.5}Se_{1.5} (BSTS) films have been grown on Al₂O₃, GaAs, MgO and Si substrates using pulsed laser deposition (PLD). The target material consisted of 99.999% pure Bi, Sb, Te, and Se. The films have been grown by ablating the target with a KrF excimer laser (wavelength 248 nm) at a frequency of 2 Hz. A base pressure of 5×10^{-6} mbar has been achieved before deposition, and a partial pressure of 5×10^{-1} mbar of flowing Argon has been maintained throughout the deposition. High-quality film growth has been ensured by using an optimized substrate temperature of 230°C and a laser fluence of around 1 J cm^{-2} . After deposition, the films were annealed at the same temperature for 20 minutes to achieve high crystallinity and reduce surface roughness. The film growth has been characterized by X-ray diffraction (XRD), Raman spectroscopy and Field emission scanning electron microscopy (FESEM).

The XRD pattern of the grown film is shown in Fig. S1(a). From Fig. S1(a), we find XRD peaks at 9.34° (003), 18.32° (006), 29.20° (009), 36.68° (0012), 46.21° (0015), 56.08° (0018) and 66.35° (0021), which agrees with the values obtained previously [1, 2].

Raman spectrum with multiple lorentzian fit and FESEM images are shown in Fig. S1(b) and S1(c) respectively. Raman spectra shows peaks at 68.21 cm^{-1} (A_{1g}^1), 113.74 cm^{-1} (E_g^1) and 175.78 cm^{-1} (A_{1g}^2) that agrees with references [3, 4]. The SEM image shows uniformly distributed grains of ~ 50 -100 nm grain size.

The thickness of the BSTS films have been measured using cross-sectional SEM as shown in Fig. S2. The thicknesses are found to be (a) 11.4 ± 2.0 nm, (b) 22.5 ± 2.0 nm, (c) 53.9 ± 2.0 nm, (d) 104.3 ± 2.0 nm, (e) 191.9 ± 2.0 nm and (f) 280.2 ± 2.0 nm respectively.

Table TS1 summarises the details such as thickness, orientation, and doping of different substrates used in the experiment.

II. EXPERIMENTAL SETUP:

Time-resolved reflectivity measurements have been done using a home-built degenerate pump-probe spectroscopy setup using a Regenerative femtosecond Amplifier (RegA 9050, Coherent Inc.) operating at a central wavelength of 790 nm with a repetition rate of 250 kHz having average

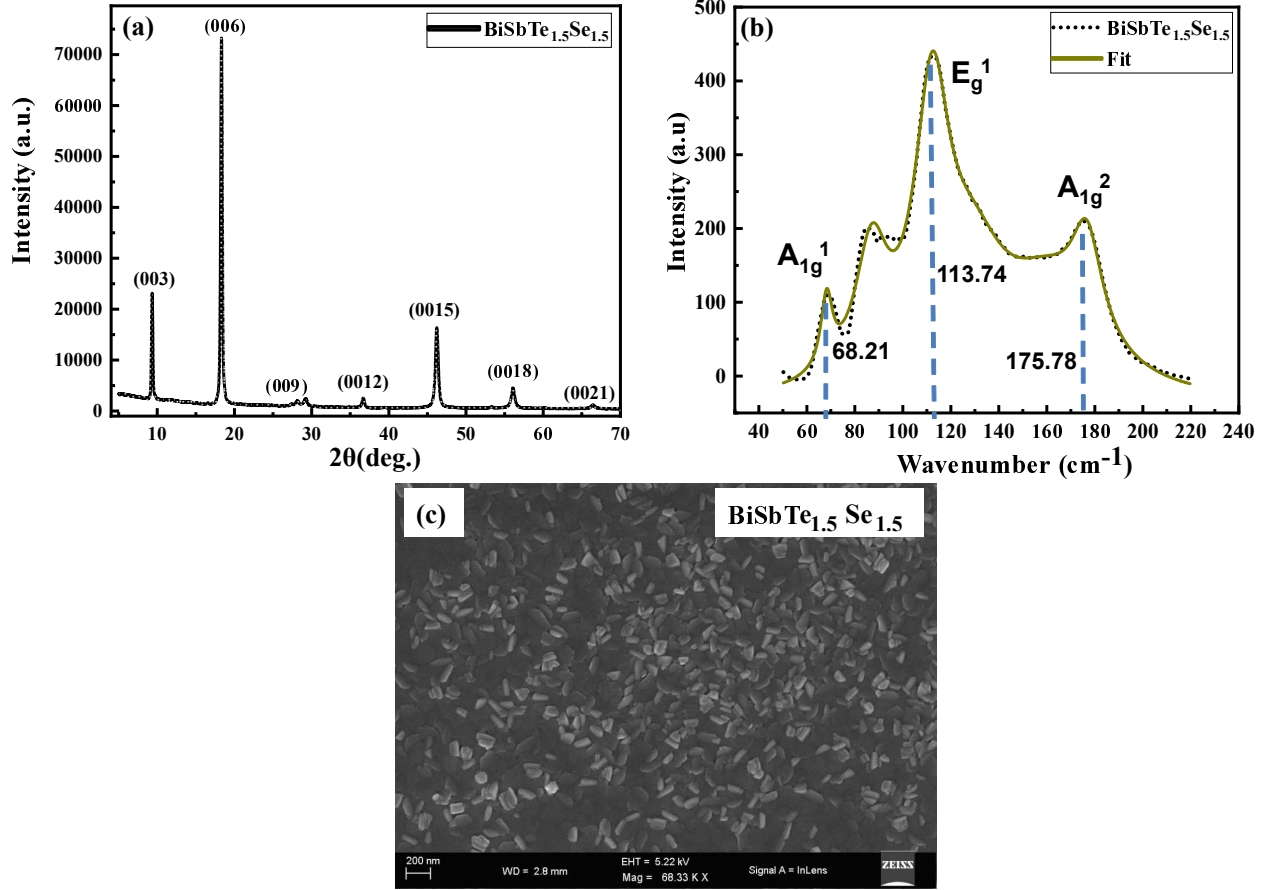


Figure S1. (a) XRD spectra (b) Raman Spectra (black dotted lines) along with multi-lorentzian fit (green solid line) (c) FESEM image for BSTS thin film.

Table TS1. Details of different substrates used for experiment.

Substrate	Orientation	Thickness (μm)	Polishing	Doping	Resistivity (ohm.cm)
Sapphire	c-plane (001)	430	Double sided polished	-	-
GaAs	<100>	485	Single sided polished	Te-doped	-
Si	<111>	280	Single sided polished	Undoped	>2000
MgO	<100>	500	Single sided polished	Undoped	-

output power of 1.6 W. Each pulse from this laser has a pulse width of 60 fs and pulse energy of 6.4 μJ . The output pulses from the RegA are split into two parts by an 80:20 beam splitter. The more intense part is used as the pump beam and less intense part as the probe beam. A variable delay stage is employed to introduce the time delay between the pump and the probe pulses at the sample

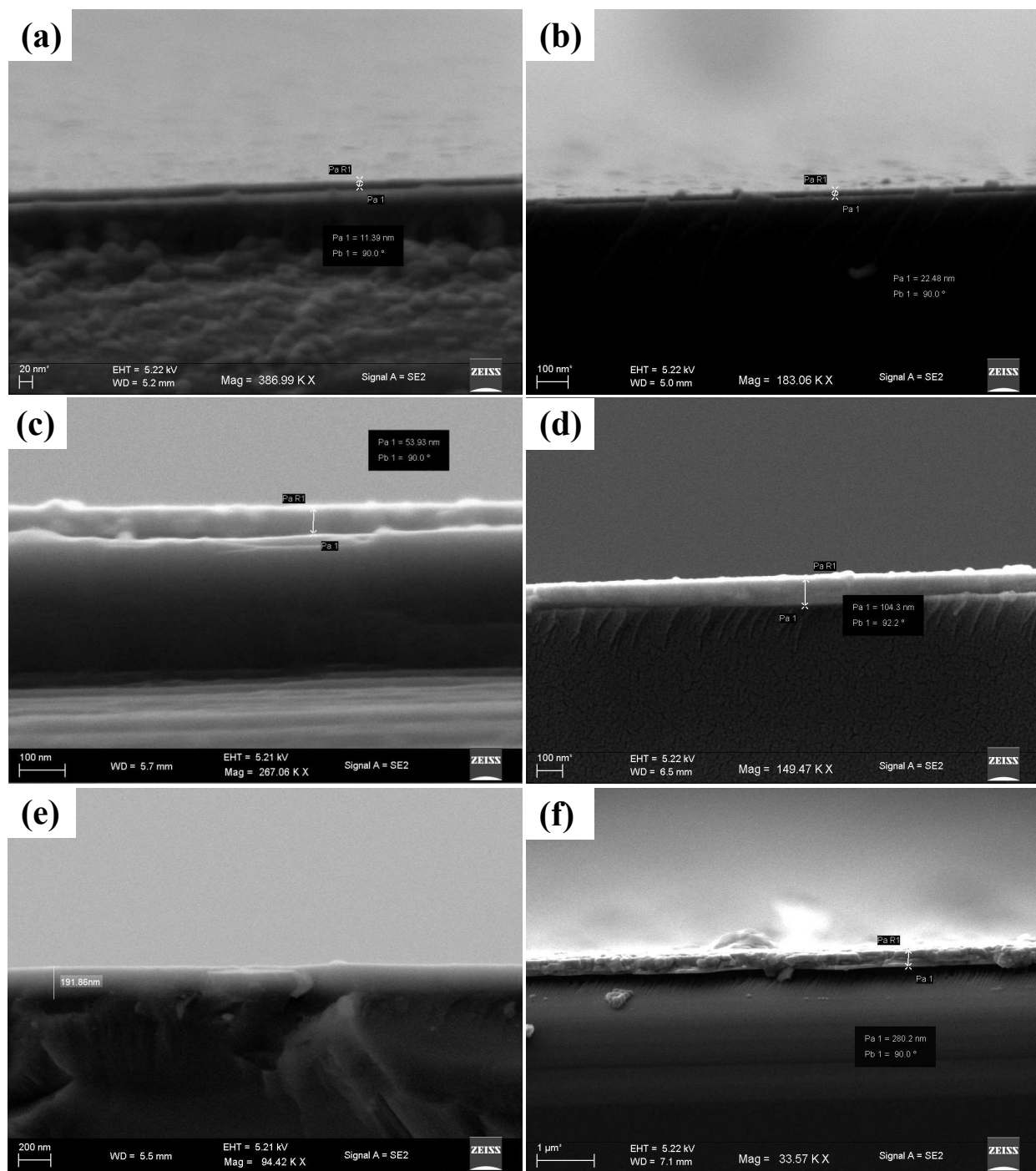


Figure S2. The Cross-sectional SEM image of BSTS films with different thickness (a) 11.4 ± 2.0 nm, (b) 22.5 ± 2.0 nm, (c) 53.9 ± 2.0 nm, (d) 104.3 ± 2.0 nm, (e) 191.9 ± 2.0 nm and (f) 280.2 ± 2.0 nm respectively.

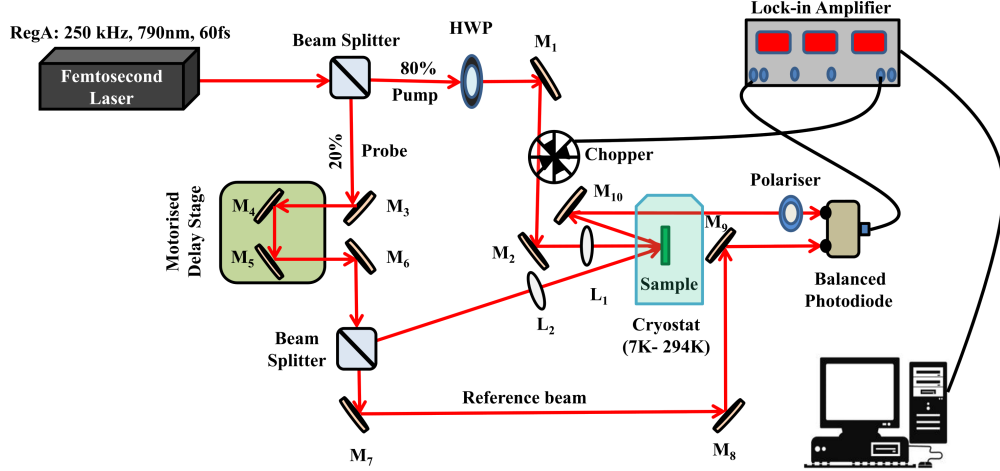


Figure S3. Schematic diagram of degenerate pump probe spectroscopy setup in reflection geometry.

location. The sample is mounted in a cryostat (Oxford OptistatDry BLV) with a temperature range of 7 K to 294 K. The transient change in the probe beam's reflectivity induced by the pump pulse is measured using balanced photo detector. A lock-in amplifier is used to achieve the phase-sensitive detection with an optical chopper modulating the pump beam at 711 Hz. To prevent scattered pump light from reaching the detector (photo-diode), a half-wave plate (HWP) is used to rotate the pump polarisation perpendicular to the probe polarisation and a polariser is used to block the pump light while allowing the probe to pass through. The pump and probe FWHM diameters are roughly $\sim 49 \mu\text{m}$ and $\sim 39 \mu\text{m}$, respectively. The pump fluence is varied from $11 \mu\text{J}/\text{cm}^2$ to $174 \mu\text{J}/\text{cm}^2$ while the probe fluence is kept constant at $6 \mu\text{J}/\text{cm}^2$. The instrument's response function, measured by the cross-correlation between the pump and probe pulses, is $\sim 235 \text{ fs}$ for our experiments. The experimental setup is shown in Fig. S3.

III. THEORETICAL MODEL:

We have adopted a theoretical approach similar to those presented by Thomsen et al. [5] and Wu et al. [6] to model the generation, propagation, and detection of travelling acoustic strain pulses (TASP) in thin films of BSTS using degenerate pump-probe spectroscopy. An intense, femtosecond laser pump pulse with the central photon energy ($\sim 1.57 \text{ eV}$) above the material band gap ($\sim 0.3 \text{ eV}$ here in BSTS) generates both the thermoelastic (σ_T) and deformation potential (σ_e) stresses at the sample surface which launches a strain pulse propagating with the sound velocity in the material (see schematic in Fig. S4). The stresses induced by each mechanism can be

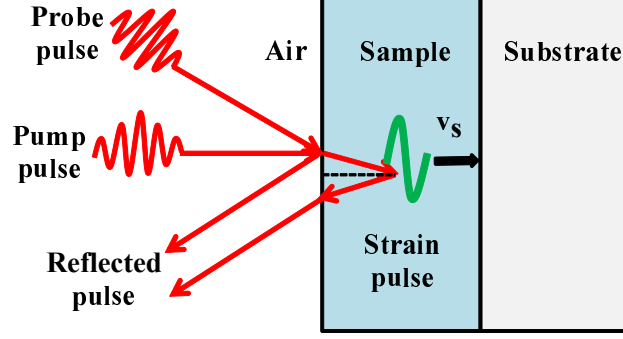


Figure S4. Schematic for the strain pulse generation and propagation

considered separately and the total stress (σ_{zz}) is just a simple sum of the electronic and thermal stresses [7]:

$$\sigma_{zz}(z, t) = \sigma_l(z, t) + \sigma_e(z, t) \quad (3)$$

$$\sigma_{zz}(z, t) = -B \left[3\beta\Delta T(z, t) + \frac{\partial E_g}{\partial P} n(z, t) \right] \quad (4)$$

where B is the bulk modulus, β is the linear thermal expansion coefficient, E_g is the band gap, and P is the pressure; $\Delta T(z, t)$ and $n(z, t)$ are the temperature rise and photo-excited carrier density, respectively.

The wave equation for describing the generation and propagation of the strain is given by [6],

$$\frac{\partial^2 \eta_{zz}}{\partial t^2} - v_s^2 \frac{\partial^2 \eta_{zz}}{\partial z^2} = \frac{1}{\rho} \frac{\partial^2 \sigma_{zz}}{\partial z^2}. \quad (5)$$

Here, ρ is the density of the material and v_s is the longitudinal sound velocity, which is expressed as $v_s^2 = \frac{3B}{\rho} \left(\frac{1-p}{1+p} \right)$. Here, p is the poisson's ratio. After putting the $n(z, t)$, $\Delta T(z, t)$ and $\sigma_{zz}(z, t)$ distributions, one can numerically solve [6] the eq. (5), subject to the initial, $t = 0$ and elastic boundary, $z = 0$ conditions (eq. (6) and eq. (7)) to obtain the strain equation.

$$\eta_{zz}(z, 0) = 0, \quad (6)$$

$$\eta_{zz}(0, t) = \frac{1}{\rho v_s^2} [3B\beta\Delta T(0, t) - a_{cv}n(0, t)] \quad (7)$$

where, $a_{cv} = -B \frac{\partial E_g}{\partial P}$ is the relative deformation potential coupling constant, defined by the difference between the coupling constants a_c and a_v of the conduction and valence bands. This

strain ($\eta_{zz}(z,t)$) is combination of the strain due to thermal expansion near the surface and travelling strain propagating away from surface with the longitudinal speed of sound [5] (v_s)(shown in Fig. S5 (a)). It is important to note that the amplitude of strain is affected by both thermal and electronic stresses, depending on strength of their respective stresses.

This propagating strain modifies the dielectric constant ($\epsilon = (n + i\kappa)^2$), which in turn changes the reflectivity (ΔR) of the film. A time-delayed probe pulse measures these reflectivity changes at the surface of the film. Therefore, the change in reflectivity ΔR upto first order in strain is given as [5, 6]:

$$\Delta R(t) = \int_0^\infty f(z)\eta_{zz}(z,t)dz, \quad (8)$$

where,

$$f(z) = f_0 \left[\frac{\partial n}{\partial \eta_{zz}} \sin\left(\frac{4\pi n z}{\lambda} - \phi\right) + \frac{\partial \kappa}{\partial \eta_{zz}} \cos\left(\frac{4\pi n z}{\lambda} - \phi\right) \right] e^{-z/\xi}, \quad (9)$$

$$f_0 = 8 \frac{\omega [n^2(n^2 + \kappa^2 - 1)^2 + \kappa^2(n^2 + \kappa^2 + 1)^2]^{1/2}}{c[(n+1)^2 + \kappa^2]^2}, \quad \& \quad (10)$$

$$\phi = \tan^{-1} \left[\frac{\kappa(n^2 + \kappa^2 + 1)}{n(n^2 + \kappa^2 - 1)} \right] \quad (11)$$

where $f(z)$ is the sensitivity function, λ is the light wavelength in free space, n and κ are real and imaginary part of complex refractive index, ξ is the absorption length ($\xi = c/2\omega\kappa$) and ϕ lies between 0 and $\pi/2$. The general form of $f(z)$ is an exponentially-damped oscillation with non zero phase at the surface i.e. at $z = 0$ (shown in Fig. S5 (b)). Parameters used for the simulation are listed in table TS2.

The ratio [5] between the deformation potential stress (σ_e) and thermo-elastic stress (σ_l) can be determined by,

$$\frac{\sigma_e}{\sigma_l} = \frac{C_l}{3\beta(E - E_g)} \frac{dE_g}{dP} \quad (12)$$

where β is linear thermal expansion coeff., C_l is specific heat and $\frac{dE_g}{dP}$ is the change of band gap energy with pressure. Using the same parameters as Bi_2Te_3 [13, 14] ($\beta \sim 4.9 \times 10^{-5} \text{ K}^{-1}$, $C_l \sim 124.4 \text{ JK}^{-1}\text{mol}^{-1}$ and $\frac{dE_g}{dP} \sim 2 \text{ meV/kbar}$) for BSTS, we obtain, $\frac{\sigma_e}{\sigma_l} \sim 0.065$ which indicates that the thermoelastic stress has a dominant role in generating the strain.

Table TS2. Parameters used for the simulation

Parameters	Values
Refractive index, n [8]	5
Penetration depth, ξ (nm) [9]	26
Mass density, ρ_m (g/cm ³) [10]	6.87
Longitudinal sound velocity, v_s (m/s)	2650
Bulk modulus, B (GPa) [9]	37
Thermal expansion coeff., β (K ⁻¹) [9]	4.9×10^{-5}
Specific heat, C (JK ⁻¹ mol ⁻¹) [9]	124.4
Deformation pot. for electrons and holes [11], d_c and d_v (eV)	22 and 25
Ambipolar diffusion constant, D_a (cm ² s ⁻¹) [12]	500
Thermal diffusion constant, D (cm ² s ⁻¹) [12]	1.2

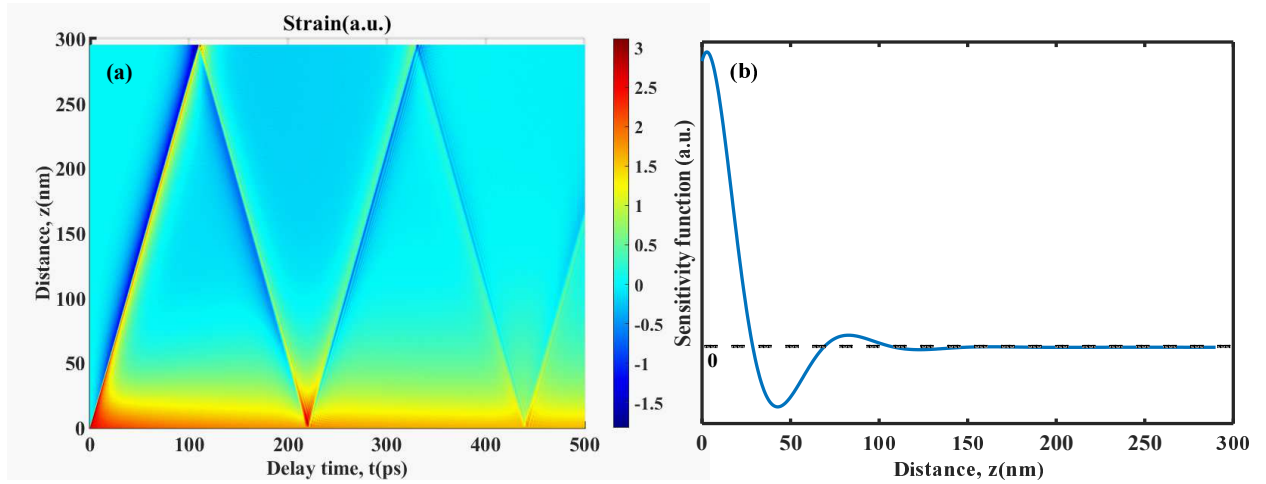


Figure S5. (a) The strain as a function of distance (z) and time delay (t) and (b) The sensitivity function as a function of z .

IV. ACOUSTIC REFLECTION COEFFICIENT:

The longitudinal sound velocity in the BSTS film can be calculated by using the thickness of the film (d) and time separation between the echo pulses ($T' = t_2 - t_1$, see Fig. S6) which is found to be $2650 \text{ m/s} \pm 36 \text{ m/s}$ using the formula $v_s = 2d/T'$ in close agreement with 2600 m/s measured previously [15] for Bi_2Te_3 .

The reflection coefficient of these acoustic strain pulses (see the insets of Fig. 1) at the sub-

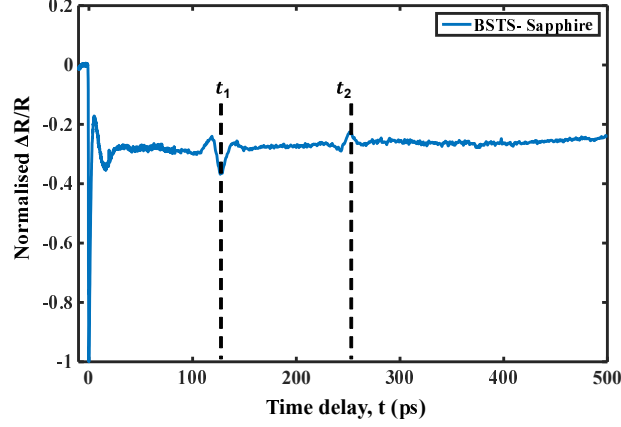


Figure S6. Time-resolved $\Delta R/R$ signal observed in BSTS thin film. Here t_1, t_2 represents the arrival time of the first and second echo of the strain pulse.

merged interface between the BSTS film and different substrates can be determined by acoustic mismatch theory [5], using the formula,

$$r_a = \frac{Z_{Substrate} - Z_{BSTS}}{Z_{Substrate} + Z_{BSTS}} \quad (13)$$

Here, r_a is acoustic reflection coefficient, Z_{BSTS} ($Z_{Substrate}$) is the acoustic impedance of BSTS (Substrate). $Z_{BSTS} = \rho_{BSTS} v_{BSTS}$ and $Z_{Substrate} = \rho_{Substrate} v_{Substrate}$ where ρ_{BSTS} ($\rho_{Substrate}$) is the density of BSTS (Substrate) and v_{BSTS} ($v_{Sapphire}$) is the longitudinal sound velocity in BSTS (Substrate). The densities of the BSTS [10], Sapphire [16], GaAs [17], MgO [19] and Si [18] are 6.87 g/cm^3 , 3.98 g/cm^3 , 5.31 g/cm^3 , 3.58 g/cm^3 and 2.33 g/cm^3 respectively. And the sound velocities for Sapphire [16], GaAs [17], MgO [19] and Si [18] are $\sim 11250 \text{ m/s}$, $\sim 4683 \text{ m/s}$, $\sim 9000 \text{ m/s}$ and $\sim 9133 \text{ m/s}$ respectively. The calculated values using eq. (13) are listed in Table TS3.

V. EXTRACTION OF EXPONENTIAL BACKGROUND FOR ALL THICKNESSES :

The time-resolved reflectivity data has been fitted with the bi-exponential model for 11 nm and 22 nm BSTS films, and single-exponential model for 54 nm, 104 nm, 192 nm and 280 nm films and the extracted parameters are shown in table TS4. After subtracting the exponential background, the fast Fourier (FFT) intensity is plotted in insets of Fig. 2 in the main manuscript. For higher thickness, 54 nm - 280 nm, after subtracting the exponential background, time- domain data is cut

Table TS3. List of calculated acoustic impedance for air, BSTS, sapphire, GaAs, Si and MgO; and acoustic reflection coefficient between the film and substrate.

Material	Acoustic Imp. ($kgm^{-2}s^{-1}$)	Acoustic Ref. Coeff. (r_a)
Air	413	
BSTS	1.82×10^7	
Sapphire	4.48×10^7	0.42
GaAs	2.48×10^7	0.15
MgO	3.22×10^7	0.28
Si	2.13×10^7	0.08

Table TS4. Extracted decay amplitudes and decay time constants for all the BSTS films

Thickness (nm)	A_0 (%)	A_1 (%)	A_2 (%)	τ_1 (ps)	τ_2 (ps)
11	14	68	17	2.0	263
22	14	73	13	2.3	380
54	27	73	-	2.1	-
104	14	86	-	2.5	-
192	16	84	-	2.2	-
280	23	76	-	2.6	-

and FFT is done only for the first echo of the acoustic strain pulse. The bi-exponential background for the lower thicknesses (e.g. 22 nm) is dominant as compared to that of higher thicknesses (e.g. 192 nm) where only the fast single exponential background is present. (see Fig. S7).

VI. TTM AND MODIFIED TTM MODEL FOR THE 22 nm FILM :

Using the two-temperature model (TTM) [20], the electron-phonon relaxation time is represented as:

$$\tau_{e-ph} = \frac{\gamma T_e^2 - T_l^2}{2H(T_e, T_l)} \quad (14)$$

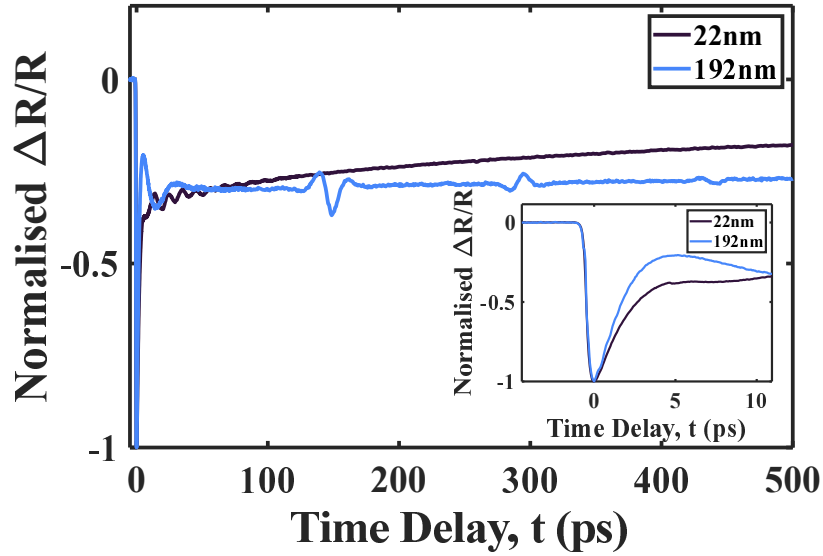


Figure S7. The time-resolved reflectivity data for 22 nm and 192 nm BSTS films. Inset shows the enlarged view of the data.

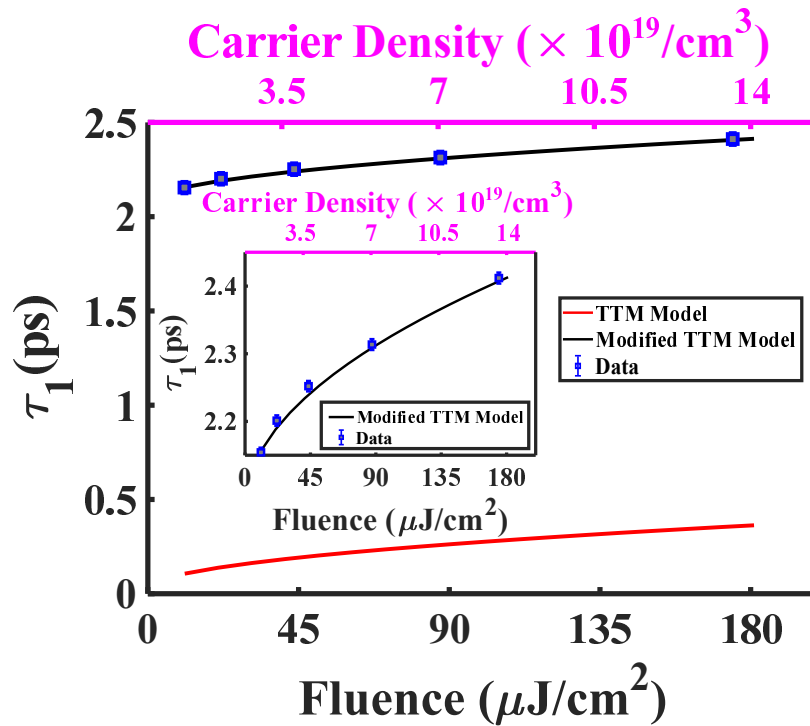


Figure S8. The variation of the fast decay constant τ_1 with the pump fluence (the corresponding carrier densities are shown on the top axis). Here, the blue open squares are the data, the red and black solid lines are the fit using normal and the modified TTM [20]. Inset shows the enlarged view of the modified TTM fit.

where γ is the electronic specific heat, T_e is the electron temperature, $T_l \approx 294$ K is the lattice temperature and $H(T_e, T_l)$ is the energy transfer function and is given by,

$$H(T_e, T_l) = f(T_e) - f(T_l) \quad (15)$$

where

$$T_e = (T_l^2 + \frac{2U_l}{\gamma})^{1/2} \quad (16)$$

and

$$f(\bar{T}) = 4g_\infty \frac{\bar{T}^5}{\theta_D^4} \int_0^{\theta_D} \frac{x^4}{e^x - 1} dx \quad (17)$$

Here, θ_D represents the Debye temperature, g_∞ is the electron-phonon coupling constant, and U_l is the deposited energy density. The TTM model is used to explain τ_1 for the 22 nm film at the room-temperature. As shown in Fig. S8, the TTM (eq. (14)) exhibits a significant deviation from the experimental data. To address this, we modified the TTM (eq. (18)) by incorporating an additional time constant into the existing model. As seen in the inset of Fig. S8, the modified TTM provides a much better fit to the experimental data.

$$\tau_{e-ph(modified)} = \tau_{e-ph} + \tau_0 \quad (18)$$

where τ_0 is an additional time constant. θ_D , g_∞ , U_l , τ_0 have been used as fitting parameters and the best fitting results have been obtained with $\theta_D = 156$ K, $g_\infty = 3.7 \times 10^{16}$ Wm⁻³K⁻², $\gamma = 4.8$ Jm⁻³K⁻² and $\tau_0 = 2.05$ ps.

VII. FLUENCE AND TEMPERATURE-DEPENDENT PARAMETERS FOR 22 nm BSTS FILM:

The behavior of the electronic decay amplitudes at various carrier densities at room temperature are shown in Fig. S9 (a)-(b). It is observed that A_1 dominates the decay process, contributing approximately 70-78%, while A_0 and A_2 contribute around 12-14% and 11-15%, respectively. A_1 represents the strength of the electron-phonon coupling and carrier diffusion, and it decreases by about 10% as the carrier density increases. A_0 , associated with direct electron-hole recombination, increases with rising carrier density. A_2 reflects the strength of the defect-assisted and phonon-assisted recombination processes and also increases with carrier density. The variation of the CAPs amplitude, B_{LA} and phase, ϕ_{LA} is shown in Fig. S9 (c)-(d). The amplitude of the phonon oscillation, B_{LA} , initially increases and then saturates at higher carrier densities, ranging from \sim

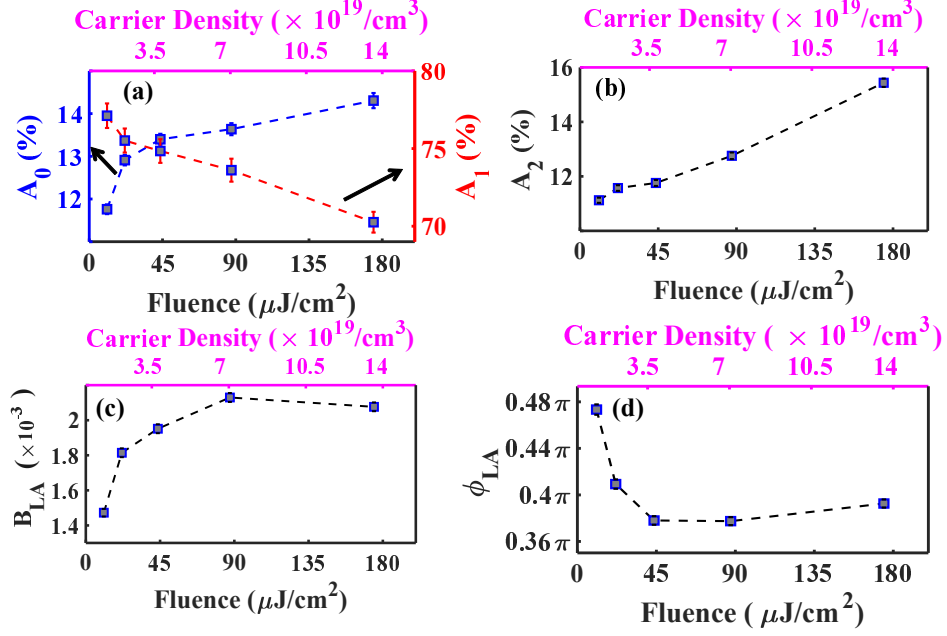


Figure S9. Pump fluence dependent variation of the fit parameters (blue open squares): (a) decay amplitudes, A_0 (left hand side), A_1 (right hand side), (b) A_2 , (c) amplitude of acoustic photons, B_{LA} and (d) phase ϕ_{LA} for 22 nm BSTS film. Top axis of all these plots display the the photo-excited carrier densities.

1.4×10^{-3} to 2.1×10^{-3} . Additionally, the phase of the phonon decreases from $\sim 0.47 \pi$ to 0.37π with increasing carrier density suggesting an sine nature at low fluences, which then changes towards cosine nature at room temperature.

Fig. S10 (a)-(b) presents the variation of the electronic decay amplitudes, A_0 , A_1 , and A_2 , as the sample is heated from 7 K to 294 K. A_0 and A_2 contributes approximately 12-18% and 12-20% with temperature. A_1 , contributing about 70-76%, increases with increase in temperature. The variation of the CAPs amplitude, B_{LA} and phase, ϕ_{LA} with temperature is shown in Fig. S10 (c)-(d). The amplitude of the acoustic phonon decreases from $\sim 2.2 \times 10^{-3}$ to 1.2×10^{-3} as temperature increases. Meanwhile, the phase of the acoustic phonon increases from approximately $\sim 0.06 \pi$ to 0.41π with increasing temperature suggesting that the acoustic phonons here, follow a sine functional behavior at room temperature, which then changes completely to the cosine behavior at 7 K. Here the photo-excited carrier density is kept constant at $\sim 1.7 \times 10^{19} \text{ cm}^{-3}$.

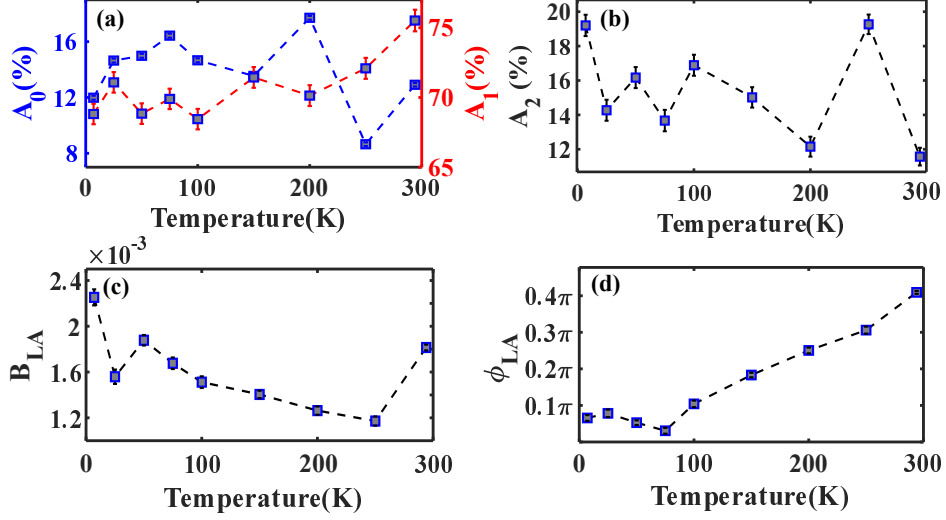


Figure S10. Temperature dependent variation of the fit parameters (blue open squares): (a) decay amplitudes, A_0 (left hand side), A_1 (right hand side), (b) A_2 , (c) amplitude of acoustic photons, B_{LA} and (d) phase ϕ_{LA} for 22 nm BSTS film. Top axis of all these plots display the the photo-excited carrier densities.

VIII. GOODNESS OF FIT VALUES:

We have fitted the transient differential reflection data for the 22 nm BSTS film with the sum of bi-exponential function and oscillatory function convoluted with a Gaussian function, using eq. (1) of the main manuscript.

$$\frac{\Delta R}{R} = (1 - e^{-t/\tau_r}) \times (A_0 + \sum_{i=1}^2 A_i e^{-t/\tau_i} + B_{LA} e^{-t/\tau_{LA}} \cos(2\pi\nu_{LA}t + \phi_{LA})) \quad (19)$$

The data and the fit are shown in Fig. 5(a) and Fig. 7(a) of the main manuscript. Goodness of fit (\mathcal{R}^2) values using eq. (20) obtained after fitting the time-resolved reflectivity (ΔR_{exp}) for the fluence and temperature-dependent data are listed in Table TS5 and TS6 respectively.

$$\mathcal{R}^2 = 1 - \frac{\sum_i [\Delta R_{exp}(i) - \Delta R_{fit}(i)]^2}{\sum_i [\Delta R_{exp}(i) - \text{mean}(\Delta R_{exp})]^2} \quad (20)$$

The carrier density can be estimated using the formula: $N = \frac{\alpha(1-R)F}{E_p}$ where " α " is the absorption coefficient, " R " is the reflection of the probe from the sample at room temperature, " F " is the

Table TS5. \mathcal{R}^2 values of the fitting for various fluences

Fluence ($\mu\text{J}/\text{cm}^2$)	Photo-excited Carrier Density ($\times 10^{19} \text{ cm}^{-3}$)	\mathcal{R}^2
11	0.8	0.9933
22	1.7	0.9933
45	3.5	0.9956
87	6.7	0.9959
174	13.5	0.9977

Table TS6. \mathcal{R}^2 values of the fitting for various temperatures

Temperature (K)	\mathcal{R}^2
7	0.9778
25	0.9750
50	0.9926
75	0.9827
100	0.9784
150	0.9924
200	0.9810
250	0.9725
294	0.9933

pump fluence and " E_p " is the central photon energy of pump pulse.

-
- [1] B. Xia, P. Ren, A. Sulaev, P. Liu, S.Q. Shen, and L. Wang, Indications of surface-dominated transport in single crystalline nanoflake devices of topological insulator $\text{Bi}_{1.5}\text{Sb}_{0.5}\text{Te}_{1.8}\text{Se}_{1.2}$, *Physical Review B—Condensed Matter and Materials Physics* **87**, 085442 (2013).
- [2] K.B. Han, S. K. Chong, A. O. Oliynyk, A. Nagaoka, S. Petryk, M. A. Scarpulla, V. V. Deshpande, and T. D. Sparks, Enhancement in surface mobility and quantum transport of $\text{Bi}_{2-x}\text{Sb}_x\text{Te}_{3-y}\text{Se}_y$ topological insulator by controlling the crystal growth conditions, *Scientific reports* **8**, 17290 (2018).
- [3] N. Kumar, N. Surovtsev, P. Yunin, D. Ishchenko, I. Milekhin, S. Lebedev, A. Lebedev, and

- O. Tereshchenko, Raman scattering spectroscopy of MBE grown thin film topological insulator $\text{Bi}_{2-x}\text{Sb}_x\text{Te}_{3-y}\text{Se}_y$, *Physical Chemistry Chemical Physics* **26**, 13497 (2024).
- [4] R. German, E. V. Komleva, P. Stein, V. G. Mazurenko, Z. Wang, S. V. Streltsov, Y. Ando, and P. H. van Loosdrecht, Phonon mode calculations and raman spectroscopy of the bulk insulating topological insulator BiSbTeSe_2 , *Physical Review Materials* **3**, 054204 (2019).
- [5] C. Thomsen, H. T. Grahn, H. J. Maris, and J. Tauc, Surface generation and detection of phonons by picosecond light pulses, *Physical Review B* **34**, 4129 (1986).
- [6] S. Wu, P. Geiser, J. Jun, J. Karpinski, and R. Sobolewski, Femtosecond optical generation and detection of coherent acoustic phonons in GaN single crystals, *Physical Review B—Condensed Matter and Materials Physics* **76**, 085210 (2007).
- [7] O. B. Wright, B. Perrin, O. Matsuda, and V. Gusev, Ultrafast carrier diffusion in gallium arsenide probed with picosecond acoustic pulses, *Physical Review B* **64**, 081202 (2001).
- [8] M. Fang, Z. Wang, H. Gu, M. Tong, B. Song, X. Xie, T. Zhou, X. Chen, H. Jiang, T. Jiang, and S. Liu, Layer-dependent dielectric permittivity of topological insulator Bi_2Se_3 thin films, *Applied Surface Science* **509**, 144822 (2020).
- [9] L. Cheng, C. Lao Vorakiat, C. S. Tang, S. K. Nair, B. Xia, L. Wang, J.X. Zhu, and E. E. Chia, Temperature-dependent ultrafast carrier and phonon dynamics of topological insulator $\text{Bi}_{1.5}\text{Sb}_{0.5}\text{Te}_{1.8}\text{Se}_{1.2}$, *Applied Physics Letters* **104**, 21 (2014).
- [10] E. Yapryntseva, O. Ivanov, A. Vasil'ev, and M. Yaprntsev, Microstructure and thermoelectric properties of medium-entropy $\text{BiSbTe}_{1.5}\text{Se}_{1.5}$ and PbSnTeSe compounds prepared by reactive spark plasma sintering, *Semiconductors* **56**, 25 (2022).
- [11] I. T. Witting, T. C. Chasapis, F. Ricci, M. Peters, N. A. Heinz, G. Hautier, and G. J. Snyder, The thermoelectric properties of bismuth telluride, *Advanced Electronic Materials* **5**, 1800904 (2019).
- [12] N. Kumar, B. A. Ruzicka, N. Butch, P. Syers, K. Kirshenbaum, J. Paglione, and H. Zhao, Spatially resolved femtosecond pump-probe study of topological insulator Bi_2Se_3 , *Physical Review B—Condensed Matter and Materials Physics* **83**, 235306 (2011).
- [13] X. Chen, H. Zhou, A. Kiswandhi, I. Miotkowski, Y. Chen, P. Sharma, A. Lima Sharma, M. Hekmaty, D. Smirnov, and Z. Jiang, Thermal expansion coefficients of Bi_2Se_3 and Sb_2Te_3 crystals from 10K to 270K, *Applied Physics Letters* **99**, 26 (2011).
- [14] S. V. Ovsyannikov, V. V. Shchennikov, G. V. Vorontsov, A. Y. Manakov, A. Y. Likhacheva, and V. A. Kulbachinskii, Giant improvement of thermoelectric power factor of Bi_2Te_3 under pressure, *Journal*

- of Applied Physics **104**, 5 (2008).
- [15] Y.Wang, C.Liebig, X.Xu, and R.Venkatasubramanian, Acoustic phonon scattering in $\text{Bi}_2\text{Te}_3/\text{Sb}_2\text{Te}_3$ superlattices, Applied Physics Letters **97**, 8 (2010).
- [16] N. Stanton and A. Kent, Propagation of high amplitude strain pulses in sapphire, Physical Review B—Condensed Matter and Materials Physics **73**, 220301 (2006).
- [17] M. Kuok, S. Ng, V. Zhang, and D. Lockwood, Acoustic mode dispersion at hypersonic frequencies in GaAs, Solid state communications **116**, 27 (2000).
- [18] I. Leibacher, S. Schatzer, and J. Dual, Impedance matched channel walls in acoustofluidic systems, Lab on a Chip **14**, 463 (2014).
- [19] X. Zhang, C. Li, F. Xu, J. Zhang, C. Gao, Z. Cheng, Y. Wu, X. Liu, A. Zerr, and H. Huang, Sound velocity anisotropy and single-crystal elastic moduli of MgO to 43 GPa, Journal of Geophysical Research: Solid Earth **128**, 6 (2023).
- [20] R. H. Groeneveld, R. Sprik, and A. Lagendijk, Femtosecond spectroscopy of electron-electron and electron-phonon energy relaxation in Ag and Au, Physical Review B **51**, 11433 (1995).